An Analytical Model for the Clear-Sky Longwave Feedback

Daniel DB Koll[1], Nadir Jeevanjee[2], and Nicholas J Lutsko[3]

[1]Peking University
[2]Geophysical Fluid Dynamics Laboratory
[3]Scripps Institution of Oceanography

November 22, 2022

Abstract

Estimates of Earth's clear-sky longwave feedback from climate models and observations robustly give a value of approximately -2 W/mˆ2/K, suggesting that this feedback can be estimated from first principles. Here we derive an analytical model for Earth's clear-sky longwave feedback based on a novel spectral decomposition that splits the feedback into components from surface emission, CO2, H2O, and the H2O continuum. Analytic expressions are given for each of these terms based on their underlying physics, and the model can also be framed in terms of Simpson's Law and deviations therefrom. We validate the model by reproducing line-by-line radiative transfer calculations across a wide range of climates, as well as the spatial dependence of the clear-sky feedback from radiative kernels. The latter result motivates us to estimate the spatial pattern of Earth's clear-sky longwave feedback from reanalysis data, which shows good agreement with climate model data. Together, these results show that Earth's clear-sky longwave feedback, its spatial variations, and its state-dependence across past and future climates can be successfully understood from only a handful of physical principles.

An Analytical Model for the Clear-Sky Longwave Feedback

Daniel D.B. Koll[a] , Nadir Jeevanjee[b] , Nicholas J. Lutsko[c]

[a] *Laboratory for Climate and Ocean-Atmosphere Studies, Dept. of Atmospheric and Oceanic Sciences; Peking University; Beijing; China*

[b] *Geophysical Fluid Dynamics Laboratory; Princeton, NJ; USA*

[c] *Scripps Institution of Oceanography; La Jolla, CA; USA*

Corresponding author: Daniel D.B. Koll, dkoll@pku.edu.cn

ABSTRACT: Estimates of Earth's clear-sky longwave feedback from climate models and observations robustly give a value of approximately -2 W m^{-2} K^{-1}, suggesting that this feedback can be estimated from first principles. Here we derive an analytical model for Earth's clear-sky longwave feedback based on a novel spectral decomposition that splits the feedback into components from surface emission, CO_2, H_2O, and the H_2O continuum. Analytic expressions are given for each of these terms based on their underlying physics, and the model can also be framed in terms of Simpson's Law and deviations therefrom. We validate the model by reproducing line-by-line radiative transfer calculations across a wide range of climates, as well as the spatial dependence of the clear-sky feedback from radiative kernels. The latter result motivates us to estimate the spatial pattern of Earth's clear-sky longwave feedback from reanalysis data, which shows good agreement with climate model data. Together, these results show that Earth's clear-sky longwave feedback, its spatial variations, and its state-dependence across past and future climates can be successfully understood from only a handful of physical principles.

SIGNIFICANCE STATEMENT: The climate feedback determines how much our planet warms due to changes in radiative forcing. For more than 50 years scientists have been predicting this feedback using complex numerical models. Except for cloud effects the numerical models widely agree, lending confidence to global warming predictions, but nobody has yet derived the feedback from simpler considerations. We show that Earth's clearsky longwave feedback can be obtained using only basic spectroscopy and atmospheric physics. Our results confirm that numerical climate models get the right number for the right reasons, and allow us to explain regional and state variations of Earth's climate feedback. These variations are difficult to understand solely from numerical models but are crucial for past and future climates.

1. Introduction

Although uncertainty in Earth's climate sensitivity is largely driven by cloud feedbacks, its magnitude is dominated by the clear-sky longwave feedback, λ_{LW}. Observational estimates and climate models give a fairly narrow range between -1.8 and -2.2 W m^{-2} K^{-1} for λ_{LW} (Andrews et al. 2012; Chung et al. 2010; Kluft et al. 2019; Zhang et al. 2020a; Zelinka et al. 2020) and even early studies estimated λ_{LW} to be -2.2-2.3 W m^{-2} K^{-1} (Manabe and Wetherald 1967; Budyko 1969), which is impressively close to the current best estimates. By contrast, the recent Sherwood et al. (2020) assessment estimated the total cloud feedback to be significantly smaller and less certain at +0.45 ± 0.33 W m^{-2} K^{-1}.

The robustness of the clear-sky longwave feedback suggests that it can be constrained from first principles. A simple model for λ_{LW}, grounded in the basic physics of radiative transfer, would provide definitive support for the value of -2 W m^{-2} K^{-1} derived from observations and climate models. It would also allow us to understand the state-dependence of λ_{LW}: at warm enough temperatures Earth's atmosphere transitions to a runaway state, in which λ_{LW} becomes zero or even changes sign, but it is unclear how λ_{LW} varies between today's value and the runaway limit. Similarly, there is a long-standing interest in using paleoclimate proxies to constrain climate sensitivity (Tierney et al. 2020), but this effort suffers from uncertainty regarding the state-dependence of climate feedbacks. At the local level, a simple model for λ_{LW} would explain the geographic variation of the local clear-sky longwave feedback and hence the contribution of the clear-sky feed-

back to the time-evolution of the global-mean climate feedback parameter in response to changing patterns of warming (Meraner et al. 2013; Armour et al. 2013; Andrews et al. 2015, 2018).

The earliest simple model for λ_{LW} was proposed by Simpson (1928), who suggested that an atmosphere that is optically thick due to water vapor absorption, but not in a runaway state, would still have a clear-sky longwave feedback that is approximately zero. Ingram (2010) resolved this "paradox" by separating out the parts of Earth's outgoing radiation spectrum that are optically thick due to water vapor (and for which λ_{LW} is approximately zero) from the optically thin "window" region. Koll and Cronin (2018) subsequently quantified Ingram's argument: using fixed relative humidity (RH), single-column calculations they showed that the net clear-sky longwave feedback is dominated by the surface component of the Planck feedback, $\lambda_{LW} \approx \lambda_{\text{surf}}$, which is simply the increase in surface emission that is able to escape to space through the spectral window. It follows that the other clear-sky longwave feedbacks – the atmospheric component of the Planck feedback, the lapse-rate feedback and the water vapor feedback – roughly cancel (Koll and Cronin 2018; Jeevanjee et al. 2021a). In a follow-up study, Zhang et al. (2020b) demonstrated that these fixed-RH results also apply to global climate model simulations, so long as the global histogram of column RH remains invariant under warming.

The match between λ_{LW} and the surface component of the Planck feedback is not exact, however. Raghuraman et al. (2019) found in radiative calculations of present-day Earth's tropics that the surface Planck feedback λ_{surf} only accounts for about 60% of λ_{LW}, implying a gap in the argument of Koll and Cronin (2018). Similarly, Seeley and Jeevanjee (2021) showed that in hot, high-CO_2 climates λ_{surf} becomes negligible yet λ_{LW} does not go to zero. As the surface warms the atmosphere is still able to increase its emission to space in spectral regions that are dominated by CO_2. This emission mostly comes from the upper atmosphere, and gives rise to a spectral CO_2 "radiator fin" feedback. The existence of the CO_2 radiator fin feedback means λ_{LW} must depend on CO_2 concentration, and thus must have CO_2 state-dependence. Moreover, because CO_2 predominantly radiates energy to space from the upper parts of the atmosphere, the magnitude of the CO_2 feedback should be sensitive to additional parameters such as the atmospheric lapse rate. So while λ_{surf} gives a reasonable first-order approximation to λ_{LW}, more terms are needed to describe λ_{LW} quantitatively.

In this study, we aim to provide a simple model of Earth's feedback that can quantitatively capture the magnitude of λ_{LW} as well as its state-dependence and regional variations. The model is derived from line-by-line radiative transfer equations, and decomposes λ_{LW} into a surface Planck feedback (λ_{surf}), a CO_2 "radiator fin" feedback (λ_{co_2}), a non-Simpsonian water vapor band feedback ($\lambda_{\text{H}_2\text{O}}$), and a destabilizing water vapor continuum feedback (λ_{cnt}). Although these feedbacks are less familiar, they represent the spectroscopic factors governing the longwave feedback, and are amenable to analysis. As shown below, expressions can be derived for each of the spectral feedbacks starting from the basic equations of radiative transfer and idealized models of H_2O and CO_2 spectroscopy. These expressions can be interpreted as a global-mean model for λ_{LW} or in terms of local feedbacks (Feldl and Roe 2013; Armour et al. 2013; Bloch-Johnson et al. 2020). That is, we treat each atmospheric column as an isolated 1D system whose longwave feedback only depends on its local surface temperature. We validate the model (and the utility of the spectral decomposition) by comparing it against two sets of calculations, one with a line-by-line radiation code and one with a radiative kernel.

Our model of λ_{LW} is based on spectroscopic thinking and hence represents a different perspective than the traditional decomposition which breaks the clear-sky longwave feedback into Planck, Lapse-rate and Water Vapor feedbacks (e.g., Soden et al. 2008; Sherwood et al. 2020; Zelinka et al. 2020). The traditional decomposition has been an invaluable tool for understanding λ_{LW} and for diagnosing the physics governing outgoing longwave radiation in climate models. However, the traditional feedback decomposition is also deceptive, since it obscures large cancellations between the atmospheric part of the Planck feedback, the Lapse-rate feedback and the Water Vapor feedback (Held and Shell 2012; Koll and Cronin 2018; Jeevanjee et al. 2021a). By obscuring the cancellations, the traditional decomposition hides the basic physics governing λ_{LW} and can give a false impression of the uncertainty of climate models. The same cancellations also make it difficult to understand the state-dependence of λ_{LW} – Planck, Lapse-rate and Water Vapor feedbacks all increase in a warmer climate, but it is far from obvious how these changes add up to affect λ_{LW}. Building on previous discussions of spectral feedbacks (e.g., Huang et al. 2010, 2014; Pan and Huang 2018; Seeley and Jeevanjee 2021; Kluft et al. 2021), our goal in this paper is to show that these issues with the traditional decomposition can be resolved by viewing λ_{LW} in terms of its spectral components instead.

The layout of the rest of this paper is as follows. Section 2 discusses several preliminaries which are necessary for the main derivations, namely: an idealized Clausius-Clapeyron relation, an analytical approximation for moist lapse rates and idealized band models for H_2O and CO_2 spectroscopy. Section 3 lays out our spectral framework and introduces the emission-level approximation, our spectral decomposition of λ_{LW}, and a description of our numerical line-by-line calculations. Section 4 derives analytical expressions for Earth's emission temperature in different parts of the spectrum, which are then used in Section 5 to derive analytical feedbacks. Our expressions compare favorably against the state-dependence of λ_{LW} from line-by-line calculations. Next, Section 6 uses these results to understand the spatial pattern of Earth's clear-sky longwave feedback. We first generate global maps of Earth's clear-sky longwave feedback using a radiative kernel plus climate model data from a preindustrial and a warmed climate. We show that our analytical expressions recover the same feedback patterns when using the same climate model data. Moreover, similar patterns can also be obtained solely from reanalysis data, which means the spatial pattern of λ_{LW} is largely predictable only using knowledge of Earth's current climate. The manuscript closes in Section 7 with a conclusion and broader discussion of the results.

2. Preliminaries

Our goal is to derive the longwave feedback of a cloud-free vertical column of atmosphere. The column's state can be specified using five parameters: T_s, γ_{lr}, RH, q_{co_2} and T_{strat}. T_s is the column's surface temperature, $\gamma_{\text{lr}} \equiv d\ln T/d\ln p$ is the column's temperature lapse rate, RH is the column relative humidity, q_{co_2} is the column's CO_2 mass mixing ratio and T_{strat} is the stratospheric temperature. We idealize the state of the vertical column by treating γ_{lr}, RH, and q_{co_2} as bulk parameters which are uniform in the vertical dimension; all are defined more precisely below. Similarly, we approximate the stratosphere as isothermal.

a. Clausius-Clapeyron

The Clausius-Clapeyron relation governs the temperature-dependence of the saturation vapor pressure $e^*(T)$ and is an essential element of our analytical model. The Clausius-Clapeyron relation is often solved by ignoring the temperature-dependence of the latent heat of vaporization,

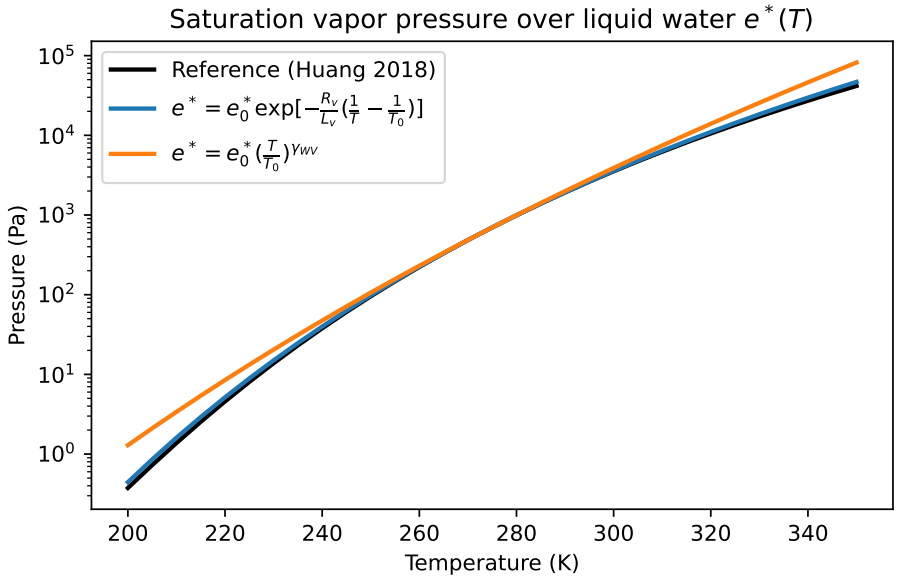

FIG. 1. Different approximations to the Clausius-Clapeyron relation. Black: fit based on experimental data (Huang 2018). Blue: the commonly-used quasi-exponential approximation. Orange: the power law approximation used in this work. The saturation vapor pressure is with respect to liquid water. In this plot (T_0, e_0^*) are set equal to the triple point values of H_2O, so $\gamma_{wv} = 19.8$.

$d \ln e^* / d \ln T = L_v(T)/(R_v T) \approx L_v(T_0)/(R_v T)$, which leads to the quasi-exponential approximation

$$e^* \approx e_0^*(T_0) \exp\left[-\frac{L_v(T_0)}{R_v}\left(\frac{1}{T} - \frac{1}{T_0}\right)\right]. \tag{1}$$

This quasi-exponential form does not lead to closed-form analytical expressions in the equations of radiative transfer, however, so we require a simpler form of the Clausius-Clapeyron relation. We obtain this by approximating the Clausius-Clapeyron relation further as $d \ln e^* / d \ln T = L_v(T)/(R_v T) \approx$ const, which leads to a simple power law between temperature and saturation vapor pressure (Koll and Cronin 2019),

$$e^* \approx e_0^*(T_0) \left(\frac{T}{T_0}\right)^{\gamma_{wv}}, \tag{2}$$

where

$$\gamma_{wv} \equiv \frac{L_v(T_0)}{R_v T_0}. \tag{3}$$

Here T_0 is an arbitrary reference temperature around which we are approximating the saturation vapor pressure as a power law. We emphasize that T_0 is effectively a thermodynamic constant and does not change with surface warming. The non-dimensional power law exponent is generally large and reflects the steep rise of e^* with temperature; at Earth-like temperatures, $\gamma_{\rm wv} \approx 20$. The fractional increase in saturation vapor pressure per unit warming is $d\ln e^*/dT = \gamma_{\rm wv}/T \sim 7\%/\mathrm{K}$, in line with other Clausius-Clapeyron approximations.

Figure 1 compares the approximations in Equations 1 and 2 against a fit that is based on experimental data (Huang 2018). Considering that a typical tropical atmospheric column spans the vertical temperature range $200-300$ K, the quasi-exponential approximation is quite accurate, whereas our power law approximation only matches more detailed fits to within a factor of two or so. Nevertheless, as shown below, this accuracy is good enough to match numerical calculations.

b. Bulk moist lapse rate

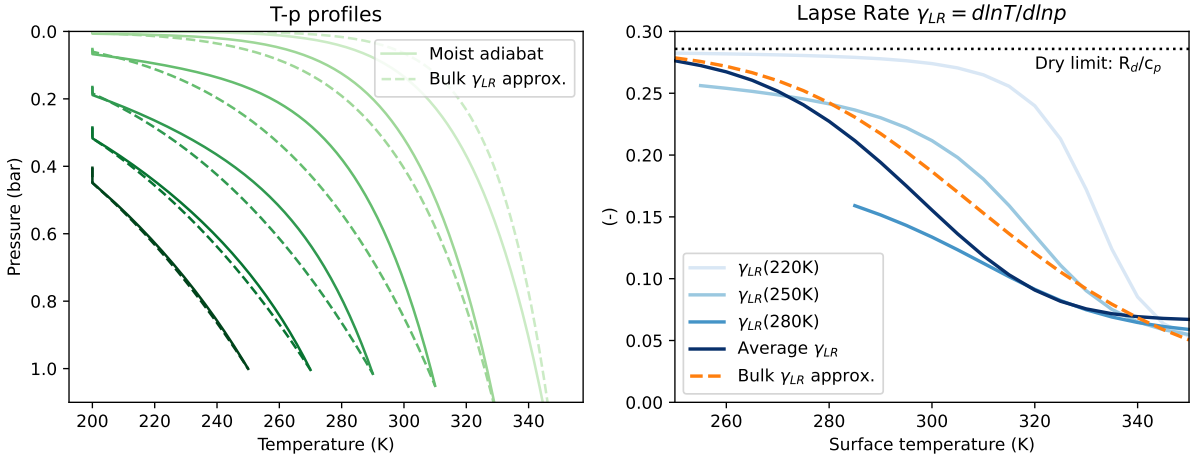

FIG. 2. Moist adiabatic lapse rates versus our analytical approximation. Left: Pressure-Temperature profiles following a moist adiabat (solid) and following the bulk lapse rate approximation (dashed). Right: numerical lapse rates computed at different temperature levels inside the troposphere (light blue), compared with the bulk approximation in Equation (8) (orange). The average of the numerical lapse rates $\gamma_{\rm lr}$ (dark blue) is a mass-weighted mean taken over the troposphere.

The vertical temperature-pressure profile of an atmospheric column can be specified via the lapse-rate exponent

$$\gamma_{\rm lr} = d\ln T / d\ln p, \tag{4}$$

where p is pressure. In the limit of a completely dry column the lapse rate exponent is vertically uniform, $\gamma_{\rm lr} = R_d/c_p \approx 2/7$. For a moist atmosphere $\gamma_{\rm lr}$ varies both as a function of temperature and pressure, but due to the latent heat release in a convecting parcel it is generally smaller than the dry lapse rate: $\gamma_{\rm lr} \leq R_d/c_p$.

In order to obtain analytically tractable expressions we would like to treat $\gamma_{\rm lr}$ as constant in the vertical even for a moist column, so we diagnose a bulk γ_{lr} using the surface and tropopause values of (T, p):

$$\gamma_{\rm lr} \approx \frac{\ln(T_{\rm tp}/T_{\rm s})}{\ln(p_{\rm tp}/p_s)}. \tag{5}$$

Assuming that the tropopause temperature stays constant in response to surface temperature changes, in accord with the FAT/FiTT hypothesis (Hartmann and Larson 2002; Seeley et al. 2019), then all that is needed is an expression for how $p_{\rm tp}$ depends on $T_{\rm s}$. We can derive such an expression by first obtaining an expression for the tropopause height $z_{\rm tp}$, following Romps (2016). From MSE conservation along an undilute moist adiabat between the surface and tropopause,

$$z_{\rm tp} \approx \frac{1}{g}\left(c_p(T_{\rm s} - T_{\rm tp}) + L_v q_s^*\right), \tag{6}$$

where q_s^* is the mass mixing ratio of water at saturation, q^*, evaluated at the surface and we neglect q^* at the tropopause. $p_{\rm tp}$ can then be obtained as

$$p_{\rm tp} = p_s e^{-z_{\rm tp}/H}, \tag{7}$$

where H is the scale height of pressure ($= \frac{R_d T_{\rm av}}{g}$) and $T_{\rm av} \equiv (T_{\rm s} + T_{\rm tp})/2$. Plugging this into (5) yields

$$\gamma_{\rm lr} \approx \frac{R_d T_{\rm av} \ln(T_{\rm s}/T_{\rm tp})}{c_p(T_{\rm s} - T_{\rm tp}) + L_v q_s^*}. \tag{8}$$

One can show that Equation 8 correctly reduces to the dry lapse rate $\gamma_{\rm lr} = R_d/c_p$ by setting $q_s^* = 0$ and series expanding the logarithm, assuming $T_{\rm s} - T_{\rm tp} \ll T_{\rm tp}$. In practice the latter assumption is

not strictly true but the resulting deviation from the dry adiabat is small even for a 100 K difference between surface and tropopause.

According to the bulk approximation, γ_{lr} is constant in the vertical and only varies in response to climatic changes (e.g., changes in surface or tropopause temperature). We can therefore write the column's vertical temperature-pressure profile as a power law,

$$T(p) = T_s \left(\frac{p}{p_s} \right)^{\gamma_{\mathrm{lr}}}. \tag{9}$$

Figure 2 (left) compares temperature-pressure profiles based on the bulk lapse rate approximation to moist adiabatic profiles. The moist adiabats are obtained by numerically integrating a generalized form of the moist adiabat which does not approximate water vapor as a dilute substance and thus remains valid at high temperatures (Ding and Pierrehumbert 2016). The temperature profiles given by Equation 9 produce a reasonable fit to the moist adiabatic profiles, though they tend to be colder throughout most of the troposphere than the moist adiabats at surface temperatures below 340 K. The tropopause temperatures and pressures are accurately reproduced by the power law profiles.

Figure 2 (right) shows the resulting T_s-dependence of γ_{lr}. The analytical approximation captures the T_s-dependence of a numerical mass-weighted column-average γ_{lr} relatively well, though the general agreement can obscure significant differences at individual atmospheric levels. For example, our analytical approximation of γ_{lr} deviates by more than a factor of two from the moist-adiabatic γ_{lr} at the atmospheric level that corresponds to $T = 220$ K. We will show below that these details of atmospheric lapse rates do not have a major impact on Earth's longwave feedback at low surface temperatures, but they become increasingly important above ~ 300 K.

c. H_2O and CO_2 spectroscopy

The third ingredient for our derivations is a model of H_2O and CO_2 spectroscopy. We follow previous studies and model the absorption cross-sections of H_2O and CO_2 as log-linear band shapes. Despite the simplicity of these models, they are able to explain numerous features of Earth's climate, including the logarithmic nature of CO_2 forcing, the temperature dependence of Earth's surface feedback and the vertical structure of radiative cooling (Crisp et al. 1986; Pierrehumbert 2010; Wilson and Gea-Banacloche 2012; Koll and Cronin 2018; Jeevanjee and Fueglistaler 2020; Romps et al. 2022). Because we explore feedbacks over a wide range of temperatures, we additionally

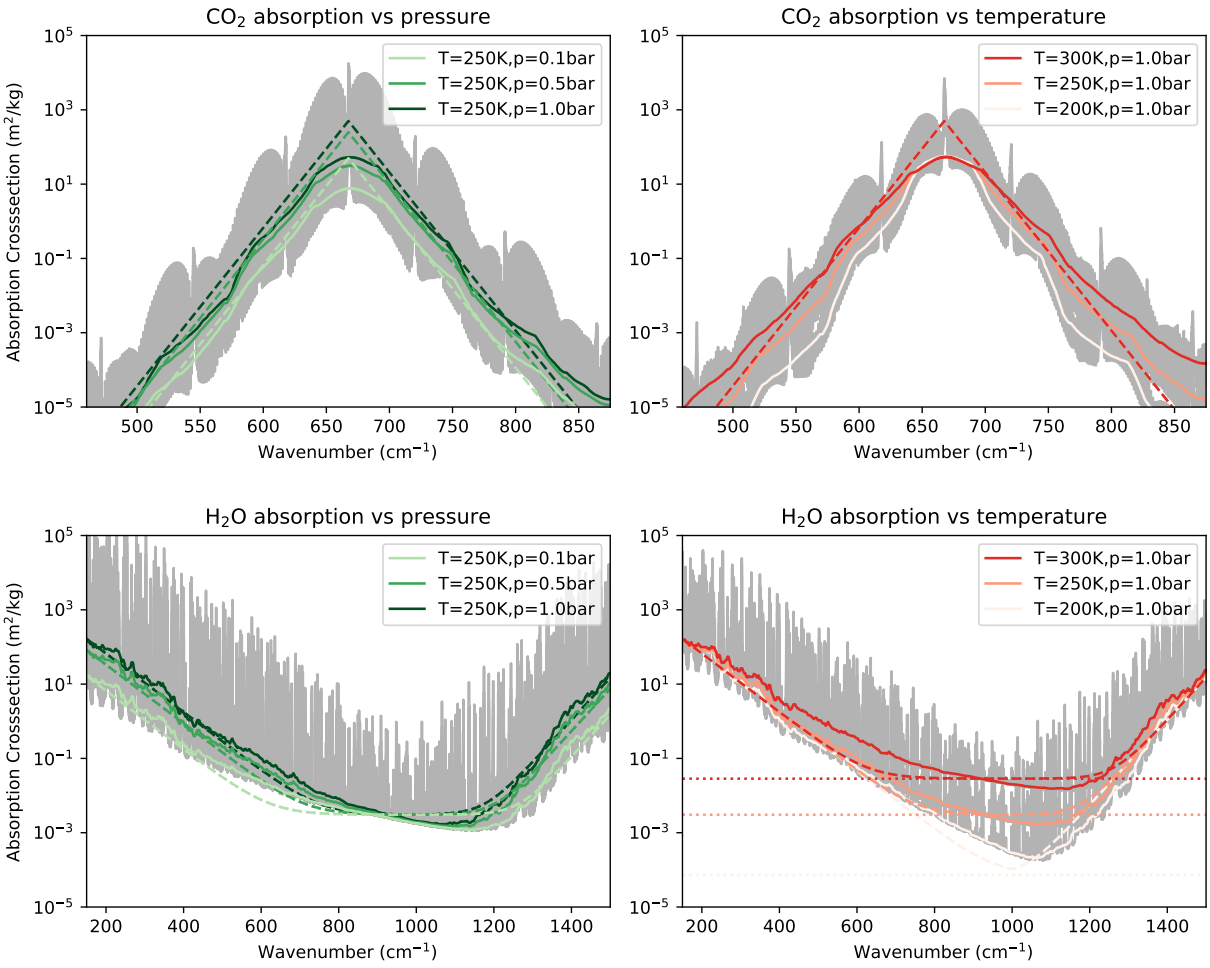

202 FIG. 3. Idealized band models compared against the absorption cross-sections of CO_2 (top row) and H_2O
203 (bottom). Grey envelopes show cross-sections computed at line-by-line spectral resolution, solid lines are the
204 cross-sections smoothed by a median filter with width 25 cm^{-1}. Dashed lines are our band models for CO_2 and
205 H_2O bands (the sum of line and continuum absorption), while dotted lines show the grey H_2O continuum model
206 only.

214 need to account for the H_2O continuum. We do so by approximating the continuum as a grey
215 absorber.

216 For CO_2 line absorption the absorption cross-section is

$$\kappa_{co_2} = \kappa_0 \left(\frac{p}{p_0}\right) \exp\left(-\frac{|\nu - \nu_0|}{l_\nu}\right), \tag{10}$$

where κ_0 is the absorption cross-section in the center of the band, p_0 is a reference pressure, ν is wavenumber, ν_0 the wavenumber of the center of the band and l_ν the decay rate of the absorption cross-section in wavenumber space. Previous work fitted these parameters to the CO_2 absorption spectrum at a reference pressure of $p_0 = 0.1$ bar (Jeevanjee et al. 2021b), here we rescale the fits to a reference pressure of $p_0 = 1$ bar. The resulting values are $\kappa_0 = 500$ m^2/kg, $\nu_0 = 667.5$ cm^{-1} and $l_\nu = 10.2$ cm^{-1}.

H_2O line absorption can similarly be modeled using a log-linear shape, though one has to account for the fact that H_2O has two bands which are relevant for Earth's longwave feedback. The rotation band determines H_2O absorption at wavenumbers less than 1000 cm^{-1}, the vibration-rotation band at wavenumbers larger than 1000 cm^{-1}. We model these two bands as

$$\kappa_{H_2O,line} = \left(\frac{p}{p_0}\right) \max\left[\kappa_{\text{rot}} \exp\left(-\frac{|\nu - \nu_{\text{rot}}|}{l_{\text{rot}}}\right), \kappa_{\text{v-r}} \exp\left(-\frac{|\nu - \nu_{\text{v-r}}|}{l_{\text{v-r}}}\right)\right]. \tag{11}$$

The factor p/p_0 in front of both H_2O and CO_2 cross-sections reflects pressure broadening: under present-Earth conditions CO_2 and H_2O absorption lines become wider due to collisions of those molecules with the background air (N_2 or O_2). This has the overall effect that both gases become more efficient absorbers at higher pressure.

In contrast to the CO_2 and H_2O bands, the H_2O continuum is dominated by self broadening so the continuum cross-section is independent of pressure and instead scales as $\propto e = \text{RH}e^*$. Although continuum absorption in reality is not uniform with respect to wavenumber, its spectral dependence is significantly weaker than the H_2O or CO_2 bands. We therefore approximate the continuum as a grey absorber and write

$$\kappa_{H_2O,cnt} = \kappa_{\text{cnt}}\, \text{RH}\, \frac{e^*(T)}{e_0^*} \left(\frac{T}{T_0}\right)^{-a}, \tag{12}$$

where the dimensionless exponent a captures the direct temperature dependence which acts to weaken the continuum (Pierrehumbert 2010). The total H_2O cross-section is the sum of line and continuum absorption, $\kappa_{H_2O} = \kappa_{H_2O,line} + \kappa_{H_2O,cnt}$. Because the line opacity decreases exponentially away from H_2O band centers, the total opacity becomes largely dominated by the continuum in the window region around ~ 1000 cm^{-1}.

Our model of H_2O spectroscopy has eight parameters: $\kappa_{\rm rot}$, $l_{\rm rot}$, $\nu_{\rm rot}$, $\kappa_{\rm v-r}$, $l_{\rm v-r}$, $\nu_{\rm v-r}$, $\kappa_{\rm cnt}$, a. We set $\nu_{\rm rot} = 150\ {\rm cm}^{-1}$ and $\nu_{\rm v-r} = 1500\ {\rm cm}^{-1}$, and fit the remaining parameters using the median-smoothed H_2O cross-sections shown in Figure 3 across the wavenumber range $150\ {\rm cm}^{-1} \leq \nu \leq 1500\ {\rm cm}^{-1}$. The results are sensitive to the smoothing procedure, that is whether one uses a geometric mean or a median. Because the average transmission across a spectral band tends to be dominated by the most optically thin frequencies (Pierrehumbert 2010), we use a median filter. To perform the fits we use the non-linear least-squares algorithm `scipy.optimize.curve_fit`, with a reference temperature of T_0=300 K. We first fit the parameters $\kappa_{\rm rot}$, $l_{\rm rot}$, $\kappa_{\rm v-r}$, $l_{\rm v-r}$ to H_2O line opacities only, and then use these parameters to fit $\kappa_{\rm cnt}$ and a to H_2O cross-sections that include both line and continuum opacity. The resulting values are $\kappa_0 = 165\ {\rm m}^2/{\rm kg}$, $l_0 = 55\ {\rm cm}^{-1}$, $\kappa_1 = 15\ {\rm m}^2/{\rm kg}$, $l_1 = 38\ {\rm cm}^{-1}$, $\kappa_{\rm cnt} = 3 \times 10^{-3}\ {\rm m}^2/{\rm kg}$ and $a = 7$, which broadly match the H_2O fits previously reported in Jeevanjee and Fueglistaler (2020). Table 1 summarizes the thermodynamic and spectral parameters used in this paper.

Figure 3 compares the idealized band models with line-by-line absorption cross-sections. Overall, the shape of the cross-sections is captured fairly well. The median CO_2 and H_2O cross-sections scale linearly with total pressure, as expected for pressure-broadening. The increasing H_2O absorption in response to warming around 1000 ${\rm cm}^{-1}$ is also qualitatively captured by our grey continuum model, even though the H_2O continuum itself is actually not grey.

Figure 3 (right plots) also shows that the slopes of the CO_2 and H_2O bands flatten as temperature increases, with roughly constant opacity in the band centers but increasing opacity in the band wings. This behavior is not captured by our simple models. Physically, absorption band slopes can depend on temperature due to the shifting population of different molecular excitation states. For example, the wings of the 667 ${\rm cm}^{-1}$ CO_2 band consist of multiple smaller bands that correspond to transitions between excited states of CO_2 (so-called hot bands). In contrast, the center of the CO_2 band is dominated by transitions to/from the ground state of CO_2. As temperature rises more CO_2 molecules leave the ground state and access excited states, which increases the probability of transitions involving excited states, which in turn preferentially increases the opacity in the wings of the CO_2 band. To keep our parameterizations simple, however, we do not attempt to model the temperature dependence of the band slopes.

TABLE 1. List of parameters and, where applicable, assumed values.

Parameter name	Explanation	Assumed value
Thermodynamic parameters		
T_0	Reference temperature for saturation vapor pressure power-law	300 K
γ_{wv}	Exponent in saturation vapor pressure power-law	18
γ_{lr}	Exponent in bulk lapse rate temperature-pressure power-law	Fit to data, or computed using Eqn. 8
Spectral parameters		
p_0	Reference pressure for absorption cross-sections	1bar
κ_0	Absorption cross-section in center of CO_2 band	500 m^2/kg
ν_0	Wavenumber of the center of the CO_2 band	667.5 cm^{-1}
l_ν	Decay rate of the CO_2 absorption cross-section in wavenumber space	10.2 cm^{-1}
κ_{rot}	Absorption cross-section in center of H_2O rotation band	165 m^2/kg
ν_{rot}	Wavenumber of the center of the H_2O rotation band	150 cm^{-1}
l_{rot}	Decay rate of the H_2O absorption cross-section in wavenumber space in the rotation band	55 cm^{-1}
$\kappa_{\mathrm{v-r}}$	Absorption cross-section in center of H_2O vibration-rotation band	15 m^2/kg
$\nu_{\mathrm{v-r}}$	Wavenumber of the center of the H_2O vibration-rotation band	1500 cm^{-1}
$l_{\mathrm{v-r}}$	Decay rate of the H_2O absorption cross-section in wavenumber space in the vibration-rotation band	38 cm^{-1}
κ_{rot}	Grey absorption cross-section of H_2O continuum	3×10^{-3} m^2/kg
a	Exponent of H_2O continuum temperature dependence	7
Analytic model parameters		
T_{strat}	Stratospheric temperature	200 K
c_{surf}	Scaling constant for surface feedback	0.8 (bulk lapse rate)/0.8 (moist adiabat)
$c_{\mathrm{H_2O}}$	Scaling constant for H_2O feedback	0.6 (bulk lapse rate)/1.0 (moist adiabat)
c_{cnt}	Scaling constant for continuum feedback	0.4 (bulk lapse rate)/0.4 (moist adiabat)
$c_{\mathrm{co_2}}$	Scaling constant for CO_2 feedback	0.7 (bulk lapse rate)/0.9 (moist adiabat)

3. Spectral Framework

a. The emission-level approximation

To decompose the net longwave feedback into multiple spectroscopic feedbacks we first need to consider the spectrally-integrated outgoing longwave flux (OLR) of a vertical column. Using the monochromatic optical thickness τ as the vertical coordinate, which varies from $\tau = 0$ at the TOA to $\tau = \tau_{LW}$ at the surface, and the wavenumber ν as the spectral coordinate, OLR is equal to (e.g. Pierrehumbert 2010)

$$\mathrm{OLR} \;=\; \int_0^\infty \pi B_\nu(T_s) e^{-\tau_{LW}}\, d\nu + \int_0^\infty \int_0^{\tau_{LW}} \pi B_\nu(T(\tau)) e^{-\tau}\, d\tau\, d\nu. \tag{13}$$

The optical thicknesses τ and τ_{LW} are functions of ν, so the order of integration cannot be switched. Physically, the first term corresponds to the surface's emission to space, while the second term corresponds to an integral of the emission coming from each vertical level in the atmosphere.

The emission-level or radiating-level approximation states that the atmosphere's emission to space (the second integral in Equation 13) originates from the vertical level at which optical thickness τ is order unity. The intuition behind the emission-level approximation is that levels of the atmosphere for which $\tau \ll 1$ are so optically thin that they do not contribute much to the TOA flux, while most emission from levels with $\tau \gg 1$ is absorbed by the overlying atmosphere and so its contribution to the TOA flux is also small. The emission level has been defined at slightly different values of τ, but all definitions agree on a value that is of order unity (Pierrehumbert 2010; Jeevanjee et al. 2021b). For simplicity, we define the emission level here as the level at which $\tau = 1$. The temperature at this level is then the emission level temperature, $T_{\text{rad}} \equiv T(\tau = 1)$, so

$$\text{OLR} \approx \int_0^\infty \pi B_\nu(T_s) e^{-\tau_{LW}} \, d\nu + \int_0^\infty \pi B_\nu(T_{\text{rad}}(\nu)) \, d\nu. \tag{14}$$

Given the emission-level approximation, the clear-sky longwave feedback is determined by how the surface emission and the atmospheric emission change in response to warming,

$$\begin{aligned} -\lambda_{LW} &= \frac{d\text{OLR}}{dT_s} \\ &\approx \int_0^\infty \pi \frac{dB_\nu}{dT}|_{T_s} e^{-\tau_{LW}} d\nu + \int_0^\infty \pi \frac{dB_\nu}{dT}|_{T_{\text{rad}}} \frac{dT_{\text{rad}}}{dT_s} d\nu. \end{aligned} \tag{15}$$

The minus sign ensures consistency with the sign convention used in most climate studies: OLR typically increases in response to surface warming, so $\lambda_{LW} < 0$. Note that Equation 15 does not contain any terms $\propto d\tau_{LW}/dT_s$ because the resulting contribution to change in the surface emission decreases with warming at exactly the same rate as the atmospheric emission increases (this can be seen by differentiating Eqn. 13 first before applying the emission-level approximation).

b. Spectral feedback decomposition

The net feedback in Equation 15 can be decomposed into multiple spectral regions or bands. The surface term dominates in the window region where $\tau_{LW} < 1$ and the feedback is primarily a function of surface temperature T_s. The atmospheric emission dominates where $\tau_{LW} > 1$, and its magnitude primarily depends on the derivative dT_{rad}/dT_s. As we show below, dT_{rad}/dT_s differs depending on the opacity source at a given wavenumber, so we split the spectral integral into four

terms:

$$
\begin{aligned}
-\lambda_{LW} &= \int_{\text{surf}} \pi \frac{dB_\nu}{dT}|_{T_s} e^{-\tau_{LW}} d\nu + \int_{\text{co}_2} \pi \frac{dB_\nu}{dT}|_{T_{\text{co}_2}} \frac{dT_{\text{co}_2}}{dT_s} d\nu + \\
&\quad \int_{\text{H}_2\text{O}} \pi \frac{dB_\nu}{dT}|_{T_{\text{H}_2\text{O}}} \frac{dT_{\text{H}_2\text{O}}}{dT_s} d\nu + \int_{\text{cnt}} \pi \frac{dB_\nu}{dT}|_{T_{\text{cnt}}} \frac{dT_{\text{cnt}}}{dT_s} d\nu \\
&= -(\lambda_{\text{surf}} + \lambda_{\text{co}_2} + \lambda_{\text{H}_2\text{O}} + \lambda_{\text{cnt}}),
\end{aligned} \tag{16}
$$

where T_{co_2}, $T_{\text{H}_2\text{O}}$ and T_{cnt} are the emission temperatures in the CO_2 band, the H_2O band, and the H_2O continuum respectively. We refer to the four feedback terms as the surface Planck feedback (λ_{surf}), the CO_2 radiator fin feedback (λ_{co_2}), the non-Simpsonian H_2O feedback ($\lambda_{\text{H}_2\text{O}}$), and the H_2O continuum feedback (λ_{cnt}).

Our spectral decomposition complements the traditional feedback decomposition which splits λ_{LW} into Planck, Lapse-Rate, and Water Vapor (or Relative Humidity) feedbacks. The surface feedback λ_{surf} measures the OLR increase due to surface warming while keeping the atmosphere fixed. This term is identical to the surface contribution to the Planck feedback or "surface kernel" in the traditional decomposition (Soden et al. 2008). As for the atmospheric feedback, Equation 15 shows that it depends on the *total* derivative of T_{rad}, that is, on dT_{rad}/dT_s. The traditional decomposition can be interpreted as splitting the total derivative dT_{rad}/dT_s up into various partial derivatives (uniform warming versus lapse-rate versus water vapor changes), while using a single, spectrally-averaged T_{rad}. In contrast, our decomposition splits the atmosphere's feedback into three different bands, but still retains the total derivative dT_{rad}/dT_s in each band. In principle our decomposition could be split further to recover the traditional decomposition. That is, one could further decompose dT_{rad}/dT_s in each band into partial derivatives of T_{rad} that correspond to vertically-uniform warming, lapse-rate warming, and water-vapor changes – see Jeevanjee et al. (2021a) for more details. Here, however, we do not pursue this approach because our analytical expressions are general enough to predict T_{rad} and the total derivative dT_{rad}/dT_s from first principles.

We use relative humidity as the state variable throughout this paper, so the analytical results are compatible with papers that argue for the use of relative humidity in feedback decompositions instead of specific humidity (Held and Shell 2012; Jeevanjee et al. 2021a). In the fixed-RH framework the traditional Water Vapor feedback is replaced by a Relative Humidity feedback, which measures the clear-sky feedback due to RH changes. It is worth noting that the RH feedback

is small in individual climate models, and its multi-model mean is close to zero (Zelinka et al. 2020). In the derivations below we therefore treat RH as a parameter that varies according to the base state of an atmospheric column, and can thus affect λ_{LW}, but whose value is assumed constant under surface warming.

c. Line-by-line calculations

To calculate spectral feedbacks numerically we use a 1D line-by-line model, PyRADS (Koll and Cronin 2018). The model's radiative transfer includes HITRAN2016 CO_2 and H_2O absorption data as well as the H_2O component of the MTCKD continuum (Mlawer et al. 2012; Gordon et al. 2017). Calculations cover the spectral range 0.1-2500 cm^{-1} with a resolution of $\Delta\nu = 0.01$ cm^{-1}, while the vertical resolution is 50 points in log-pressure. The two-stream equations require specifying an average zenith angle for the radiative fluxes, and PyRADS assumes $\cos(\bar{\theta}) = 3/5$. To quantitatively compare our theoretical scalings against line-by-line calculations the optical thickness in all scalings therefore needs to be divided by $\cos(\bar{\theta})$ (this is equivalent to multiplying the surface gravity g by $\cos(\bar{\theta})$).

In the 1D calculations we assume the atmospheric temperature profile follows either a moist adiabat or a power law temperature-pressure profile that is consistent with our bulk lapse rate approximation. In both cases the troposphere is capped by a tropopause at 200 K, while the overlying stratosphere is isothermal at the same temperature. Relative humidity in the troposphere is vertically uniform while the H_2O mass fraction in the stratosphere is set equal to its value at the tropopause. CO_2 is treated as uniformly mixed in the vertical and fixed with respect to surface temperature. Because we are considering a wide range of surface temperatures, across which the tropopause pressure varies substantially, we vary the vertical grid-spacing in PyRADS. The model top pressure is set to a slightly lower value than the estimated tropopause pressure based on our bulk lapse rate formulation, which ensures the model's top is always in the stratosphere and the tropopause is well resolved.

The spectrally-resolved feedback is the difference in the spectrally-resolved outgoing longwave flux, OLR_ν, between a base state and a perturbed state with warmed surface and atmosphere,

$$-\lambda_\nu = \frac{\mathrm{OLR}_\nu(T_s + \Delta T_s, \vec{T} + \Delta\vec{T}) - \mathrm{OLR}_\nu(T_s, \vec{T})}{\Delta T_s}. \tag{17}$$

We use $\Delta T_s = 1$ K, while $\Delta\vec{T}$ denotes the atmospheric temperature perturbation caused by the surface warming ΔT_s. Because relative humidity is kept fixed, the atmospheric warming $\vec{T} + \Delta\vec{T}$ also implies an increase in specific humidity.

Previous work used various approaches to assign physical significance to line-by-line output. Seeley and Jeevanjee (2021) defined CO_2 versus H_2O bands based on the column-integrated, spectrally-smoothed optical thickness of CO_2 and H_2O. However, as we show below, the behavior of H_2O differs strongly between the H_2O bands and the H_2O continuum, and it is difficult to distinguish these terms based on column-integrated optical thicknesses. For example, the H_2O continuum might have a larger integrated optical thickness at some wavenumber than the H_2O bands, but because continuum absorption decays more rapidly with altitude than line absorption ($\kappa_{\text{cnt}} \propto e^*(T)$ versus $\kappa_{H_2O} \propto p$) the emission at the level where $\tau \sim 1$ could still be determined by the H_2O bands.

Instead we first split the net feedback into its contributions from the surface versus atmosphere. The spectrally-resolved surface feedback is the feedback in response to surface-only warming while keeping the atmosphere fixed,

$$-\lambda^{\nu}_{\text{surf}} = \frac{\text{OLR}_\nu(T_s + \Delta T_s, \vec{T}) - \text{OLR}_\nu(T_s, \vec{T})}{\Delta T_s}. \tag{18}$$

If we integrate $\lambda^{\nu}_{\text{surf}}$ over all wavenumbers we get the surface feedback λ_{surf}, equivalent to the surface kernel of Soden et al. (2008). The atmospheric feedback is equal to the difference between λ_ν and $\lambda^{\nu}_{\text{surf}}$,

$$-\lambda^{\nu}_{atm} = \frac{\text{OLR}_\nu(T_s, \vec{T} + \Delta\vec{T}) - \text{OLR}_\nu(T_s, \vec{T})}{\Delta T_s}. \tag{19}$$

We split λ^{ν}_{atm} into different bands based on the spectrally-resolved emission pressures of CO_2, H_2O, and the H_2O continuum. For each absorber PyRADS computes the optical thickness as a function of pressure and wavenumber, $\tau(p, \nu)$. We define the CO_2 emission pressure as the pressure at which the optical thickness of CO_2 is equal to unity,

$$\tau_{\text{co}_2}(p_{\text{rad}}, \nu) \quad = \quad 1, \tag{20}$$

which can be solved in each wavenumber bin to find $p_{\rm rad}(\nu)$ (in practice we interpolate to find the pressure at which $\log[\tau] = 0$). The emission pressures of H_2O and the H_2O continuum are determined for each wavenumber bin in the same manner. The CO_2 feedback $\lambda_{\rm co_2}$ is then the integral of λ^{ν}_{atm} over all wavenumbers at which CO_2 has the smallest emission pressure, the H_2O feedback $\lambda_{\rm H_2O}$ is the integral of λ^{ν}_{atm} over all wavenumbers at which H_2O has the smallest emission pressure, and so on. We note that this approach is justified if one emitter clearly dominates the atmosphere's emission at a given wavenumber, such that its emission pressure $p_{\rm rad}$ is much lower than that of any other emitters, but could be misleading if two emitters have very similar emission pressures. In practice, however, H_2O and CO_2 absorption cross-sections decrease quasi-exponentially away from their band centers (see Section 2), which means the wavenumber range over which two absorbers can have a similar emission pressure is limited.

4. Emission temperatures

The feedbacks are set by the temperatures at the $\tau = 1$ levels, so we seek analytical expressions for the emission temperatures $T_{\rm co_2}$, $T_{\rm H_2O}$ and $T_{\rm cnt}$. The optical thickness of a generic absorber is

$$\tau \;=\; \int \kappa q \frac{dp}{g}, \tag{21}$$

where κ is the absorption cross-section and q is the absorber's mass-specific concentration. We use this equation to derive expressions for the emission temperatures by first writing the optical thickness in each band as a function of atmospheric temperature, then inverting these relations to find the emission temperature at the $\tau = 1$ level.

a. CO_2

CO_2 is well-mixed in the atmosphere so its mass-specific concentration $q_{\rm co_2}$ is vertically uniform. As discussed in Section 2, its absorption cross-section depends linearly on pressure due to pressure broadening and can be written as $\kappa_{\rm co_2}(\nu, p) = \kappa^*_{\rm co_2}(\nu)(p/p_0)$. $\kappa^*_{\rm co_2}$ captures the wavenumber-dependence of the CO_2 absorption cross-section, $\kappa^*_{\rm co_2} \propto \exp(-|\nu - \nu_0|/l_\nu)$, while p_0 is an arbitrary reference pressure. For simplicity we set p_0 equal to the surface pressure p_s, so $\kappa^*_{\rm co_2}(\nu) = \kappa_{\rm co_2}(\nu, p_s)$.

The optical thickness at a vertical level with temperature and pressure (T, p) is then

$$\begin{aligned}
\tau_{\mathrm{co_2}} &= \int_0^p \kappa^*_{\mathrm{co_2}} \left(\frac{p'}{p_s}\right) q_{\mathrm{co_2}} \frac{dp'}{g}, \\
&= \frac{\kappa^*_{\mathrm{co_2}}}{2gp_s} q_{\mathrm{co_2}} p^2, \\
&= \frac{\kappa^*_{\mathrm{co_2}} p_s}{2g} q_{\mathrm{co_2}} \left(\frac{p}{p_s}\right)^2 \\
&= \frac{\kappa^*_{\mathrm{co_2}} p_s}{2g} q_{\mathrm{co_2}} \left(\frac{T}{T_s}\right)^{2/\gamma_{\mathrm{lr}}} \\
&\equiv \tau^*_{\mathrm{co_2}}(\nu)\ q_{\mathrm{co_2}} \times \left(\frac{T}{T_s}\right)^{2/\gamma_{\mathrm{lr}}}, \qquad (22)
\end{aligned}$$

where we have used the bulk lapse rate in the fourth step. Note that all spectroscopic parameters as well p_s and g are combined into a reference optical thickness, $\tau^*_{\mathrm{co_2}}(\nu)$, which encapsulates how CO_2 absorption varies with respect to wavenumber ν, surface pressure p_s, and gravity g, but which can be treated as constant in response to warming.

b. Non-Simpsonian H_2O

As for CO_2, the absorption cross-section of H_2O scales linearly with pressure and can be written as $\kappa_{\mathrm{H_2O}}(\nu, p) = \kappa^*_{\mathrm{H_2O}}(\nu)(p/p_s)$. We use the Clausius-Clapeyron power law approximation to write the saturation specific humidity as $q^* \approx R_d/R_v \times e^*_0/p \times (T/T_0)^{\gamma_{\mathrm{wv}}}$ and the specific humidity as

$q = \mathrm{RH} \times q^*$. The optical thickness of H_2O at a level (T, p) is then

$$\begin{aligned}
\tau_{\mathrm{H_2O}} &= \int_0^p \kappa^*_{\mathrm{H_2O}} \left(\frac{p'}{p_s}\right) q \frac{dp'}{g}, \\
&\approx \mathrm{RH}\ \frac{\kappa^*_{\mathrm{H_2O}} e^*_0}{g} \frac{R_d}{R_v} \times \int_0^p \left(\frac{p'}{p_s}\right) \left(\frac{T'}{T_0}\right)^{\gamma_{\mathrm{wv}}} \frac{dp'}{p'} \\
&= \mathrm{RH}\ \frac{\kappa^*_{\mathrm{H_2O}} e^*_0}{g} \frac{R_d}{R_v} \times \int_0^T \left(\frac{T'}{T_s}\right)^{1/\gamma_{\mathrm{lr}}} \left(\frac{T'}{T_0}\right)^{\gamma_{\mathrm{wv}}} \frac{1}{\gamma_{\mathrm{lr}}} \frac{dT'}{T'} \\
&= \mathrm{RH}\ \frac{\kappa^*_{\mathrm{H_2O}} e^*_0}{g} \frac{R_d}{R_v} \frac{1}{\gamma_{\mathrm{lr}}} \left(\frac{T_0}{T_s}\right)^{1/\gamma_{\mathrm{lr}}} \times \int_0^T \left(\frac{T'}{T_0}\right)^{\gamma_{\mathrm{wv}} + \frac{1}{\gamma_{\mathrm{lr}}}} \frac{dT'}{T'} \\
&= \mathrm{RH}\ \frac{\kappa^*_{\mathrm{H_2O}} e^*_0}{g} \frac{R_d}{R_v} \frac{1}{1 + \gamma_{\mathrm{wv}} \gamma_{\mathrm{lr}}} \times \left(\frac{T}{T_0}\right)^{\frac{1+\gamma_{\mathrm{wv}}\gamma_{\mathrm{lr}}}{\gamma_{\mathrm{lr}}}} \left(\frac{T_0}{T_s}\right)^{1/\gamma_{\mathrm{lr}}} \\
&\equiv \mathrm{RH}\ \tau^*_{\mathrm{H_2O}}(\nu) \frac{1}{1 + \gamma_{\mathrm{wv}} \gamma_{\mathrm{lr}}} \times \left(\frac{T}{T_0}\right)^{\frac{1+\gamma_{\mathrm{wv}}\gamma_{\mathrm{lr}}}{\gamma_{\mathrm{lr}}}} \left(\frac{T_0}{T_s}\right)^{1/\gamma_{\mathrm{lr}}}. \qquad (23)
\end{aligned}$$

where in the second step we have used the Clausius-Clapeyron power law and also replaced the water vapor concentration in the stratosphere with the water vapor concentration of a moist adiabat that extends all the way to the top-of-atmosphere. We again define a reference optical thickness, $\tau^*_{\mathrm{H_2O}}(\nu)$, which encapsulates how H_2O line absorption varies with respect to wavenumber ν, and gravity g, but which is independent of temperature.

c. H_2O Continuum

Absorption by the H_2O continuum strengthens in response to increasing water vapor concentrations and weakens in response to warming, $\kappa_{\mathrm{H_2O,cnt}} = \kappa_{\mathrm{cnt}} \times \mathrm{RH}\ e^*(T)/e^*(T_0) \times (T/T_0)^{-a}$. The

optical thickness of the continuum is then

$$\begin{aligned}
\tau_{\rm cnt} &= {\rm RH}\int_0^p \kappa_{\rm cnt}\frac{e^*(T')}{e^*(T_0)}\left(\frac{T'}{T_0}\right)^{-a} q\frac{dp'}{g}, \\
&\approx {\rm RH}^2\,\frac{\kappa_{\rm cnt}e_0^*}{g}\frac{R_d}{R_v}\times\int_0^T\left(\frac{T'}{T_0}\right)^{2\gamma_{\rm wv}-a}\frac{dp'}{p}, \\
&= {\rm RH}^2\,\frac{\kappa_{\rm cnt}e_0^*}{g}\frac{R_d}{R_v}\times\int_0^T\left(\frac{T'}{T_0}\right)^{2\gamma_{\rm wv}-a}\frac{1}{\gamma_{\rm lr}}\frac{dT'}{T'}, \\
&= {\rm RH}^2\,\frac{\kappa_{\rm cnt}e_0^*}{g}\frac{R_d}{R_v}\frac{1}{(2\gamma_{\rm wv}-a)\gamma_{\rm lr}}\times\left(\frac{T}{T_0}\right)^{2\gamma_{\rm wv}-a}, \\
&\equiv {\rm RH}^2\,\tau^*_{\rm cnt}\frac{1}{(2\gamma_{\rm wv}-a)\gamma_{\rm lr}}\times\left(\frac{T}{T_0}\right)^{2\gamma_{\rm wv}-a}, \qquad (24)
\end{aligned}$$

where the second and third step make the same assumptions as our derivation for the H_2O band. Here the reference optical thickness, $\tau^*_{\rm cnt}$ encapsulates how the H_2O self-continuum varies with respect to gravity g but has no dependence on wavenumber or temperature.

d. Emission temperatures

By setting $\tau = 1$ and inverting the above relations, we arrive at the emission temperatures in the CO_2 band, the H_2O band and the H_2O self-continuum:

$$T_{\rm co_2} = T_s\left(\frac{1}{\tau^*_{\rm co_2}(\nu)q_{\rm co_2}}\right)^{\gamma_{\rm lr}/2} \qquad (25a)$$

$$T_{\rm H_2O} = T_0\left(\frac{1+\gamma_{\rm wv}\gamma_{\rm lr}}{\tau^*_{\rm H_2O}(\nu){\rm RH}}\right)^{\frac{\gamma_{\rm lr}}{1+\gamma_{\rm wv}\gamma lr}}\left(\frac{T_s}{T_0}\right)^{\frac{1}{1+\gamma_{\rm wv}\gamma lr}} \qquad (25b)$$

$$T_{\rm cnt} = T_0\left(\frac{(2\gamma_{\rm wv}-a)\gamma_{\rm lr}}{\tau^*_{\rm cnt}{\rm RH}^2}\right)^{\frac{1}{2\gamma_{\rm wv}-a}}. \qquad (25c)$$

To interpret these emission temperatures, consider whether a given emitter stabilizes or destabilizes Earth's climate. For CO_2 it is easy to see that the feedback is always stabilizing. Ignoring lapse rate changes we have $T_{\rm co_2} \propto T_s$, so $dT_{\rm co_2}/dT_s > 0$. More intuitively, the optical thickness of CO_2 can be written as

$$\tau_{\rm co_2} \propto \left(\frac{T}{T_s}\right)^{2/\gamma_{\rm lr}} = \left(\frac{p}{p_s}\right)^2. \qquad (26)$$

The emission level of CO_2 is therefore a fixed function of pressure. Given that the atmosphere's temperature at a fixed pressure level always increases in response to surface warming, T_{co_2} also has to increase under warming. This effect can be thought of as a spectral "radiator fin", and is valid also if the lapse rate γ_{lr} varies in response to surface warming. It implies that even if the atmosphere stops emitting more at all other wavenumbers, so $dT_{\mathrm{rad}}/dT_s = 0$ outside the CO_2 band, the presence of CO_2 still allows the atmosphere to shed more energy to space in response to surface warming (Seeley and Jeevanjee 2021).

Next, our expressions suggest that the feedback from H_2O is small and, to first order, might be negligible. Equation 25b shows $T_{\mathrm{H_2O}} \propto T_s^{1/(1+\gamma_{\mathrm{wv}}\gamma_{\mathrm{lr}})}$, where representative values for Earth's tropics are $\gamma_{\mathrm{wv}} \sim 20$ and $\gamma_{\mathrm{lr}} \sim 1/7$, so the H_2O emission temperature only depends weakly on surface temperature, $T_{\mathrm{H_2O}} \propto T_s^{1/4}$. This small exponent is closely related to Simpson's "paradox" (Ingram 2010) or Simpson's "law" (Jeevanjee et al. 2021a), which state that $T_{\mathrm{H_2O}}$ is approximately independent of surface temperature. In the limit $\gamma_{\mathrm{wv}}\gamma_{\mathrm{lr}} = d\ln e^*/d\ln p \gg 1$, that is, if water vapor increases much faster in the vertical than the total atmospheric mass, then

$$T_{\mathrm{H_2O}} \approx T_0 \left(\frac{\gamma_{\mathrm{wv}}\gamma_{\mathrm{lr}}}{\tau^*_{\mathrm{H_2O}}(\nu) RH} \right)^{\frac{1}{\gamma_{\mathrm{wv}}}}, \tag{27}$$

and $T_{\mathrm{H_2O}}$ ceases to depend on T_s. If the lapse rate is also independent of T_s we recover Simpon's law:

$$\frac{dT_{\mathrm{H_2O}}}{dT_s} \approx 0. \tag{28}$$

In reality, however, water vapor dominates most of the atmospheric emission and even minor deviations from Simpson's law can have a non-negligible impact on the longwave feedback. Deviations arise because the H_2O optical thickness is sensitive to pressure broadening and because changes in γ_{lr} modify the total water vapor path inside the atmospheric column. For present-day Earth the net impact of these changes is to increase the H_2O emission temperature under surface warming, $T_{\mathrm{H_2O}} \propto T_s^{1/4}$, such that $dT_{\mathrm{H_2O}}/dT_s > 0$ which means the H_2O bands tend to stabilize Earth's climate.

Finally, $T_{\rm cnt}$ has no direct dependence on surface temperature, but is sensitive to lapse rate changes. If we take the continuum's emission temperature (Eqn. 25c), and assume that the direct temperature-dependence of the continuum $a \sim 7$ is much smaller than its temperature-dependence due to the Clausius-Clapeyron relation, $2\gamma_{\rm wv} \sim 40$, we have

$$T_{\rm cnt} \quad \propto \quad T_0 \times [\gamma_{\rm lr}]^{1/(2\gamma_{\rm wv})}. \tag{29}$$

Because the lapse rate $\gamma_{\rm lr}$ decreases under surface warming we have $dT_{\rm cnt}/dT_s = dT_{\rm cnt}/d\gamma_{\rm lr} \times d\gamma_{\rm lr}/dT_s < 0$. Physically, this effect can be understood by considering the impact of $\gamma_{\rm lr}$ on the atmosphere's total water vapor path. If one decreases the lapse rate $\gamma_{\rm lr}$ while keeping T_s fixed, the atmospheric column can store more water vapor. To still maintain an optical thickness of unity then requires that the continuum's emission level moves to colder temperatures. Our expressions thus predict that the H_2O continuum gives rise to a destabilizing feedback.

e. Comparison against LBL calculations

Equations 25a - 25c predict how Earth's emission temperature varies in response to changes in T_s, $q_{\rm co_2}$, $\gamma_{\rm lr}$ and RH. To test these equations we perform four sets of numerical experiments with PyRADS in which we variously change T_s, $q_{\rm co_2}$, $\gamma_{\rm lr}$, and RH while holding the other parameters fixed. The default values are T_s = 290 K, 400 ppm of CO_2, $\gamma_{\rm lr} = 2/7$, and RH = 0.8. To match our underlying assumptions we assume a bulk tropospheric lapse rate, so $T = T_s(p/p_s)^{\gamma_{\rm lr}}$, which means the temperature profile differs from an adiabat if $\gamma_{\rm lr} < 2/7$. The troposphere is capped by an isothermal stratosphere which is kept fixed at T_{strat} = 200 K. Note that in Equations 25a - 25c the dependence on wavenumber only enters through the reference optical thicknesses $\tau^*_{\rm co_2}$, $\tau^*_{\rm H_2O}$, and $\tau^*_{\rm cnt}$, which are evaluated using the cross-sections from Section 2. Because the cross-sections were fitted independently, the analytical $T_{\rm rad}$ expressions do not contain any free tuning parameters.

To compare the analytical results against line-by-line calculations we first numerically compute the top-of-atmosphere spectral flux $\rm OLR_\nu$ for a given set of (T_s, $q_{\rm co_2}$, $\gamma_{\rm lr}$, RH). We then smooth $\rm OLR_\nu$ with a median filter of width 50 $\rm cm^{-1}$, before inverting it using the Planck function to find the atmosphere's emission temperature (also known as brightness temperature) at a given wavenumber.

Finally, we combine our analytical expressions into a single emission temperature via

$$T_{\text{rad}} \quad = \quad \max\left[T_{strat}, \min\left[T_s, T_{\text{co}_2}, T_{\text{H}_2\text{O}}, T_{\text{cnt}}\right]\right], \tag{30}$$

to compare directly with temperatures from line-by-line calculations.

Figure 4 shows that the analytical results compare favorably against numerical calculations. Even though the analytical T_{rad} shapes are idealized compared to the numerical calculations, the overall response of T_{rad} to perturbations is captured well. First, increasing CO_2 concentration lowers T_{rad} around 667 cm^{-1}, which corresponds to the wings of the CO_2 band. This is simply a spectrally resolved view of how increasing CO_2 acts as a radiative forcing (Jeevanjee et al. 2021b). Second, warming the surface while keeping all other parameters fixed has multiple effects. The main impact is to increase the emission temperature in the window region between $\sim$ 800 and 1200 cm^{-1}. In addition there are secondary impacts: surface warming also shrinks the width of the CO_2 band and slightly increases the emission temperature in the H_2O bands below 600 cm^{-1} and above 1300 cm^{-1} (this latter effect is hard to see in Figure 4). The increased emission in the H_2O bands shows that Simpson's law in Equation 28 is not exact, an effect that is captured by our analytical expressions. Third, reducing the lapse rate γ_{lr} preserves the width of the CO_2 band, but it flattens the steepness of its slopes and increases the emission temperature in the center of the band. In the H_2O bands, a smaller γ_{lr} while keeping T_s fixed also leads to a non-Simpsonian increase of the emission temperature in the H_2O bands. In contrast to the H_2O bands, the emission temperature of the H_2O continuum around 1000 cm^{-1} decreases as γ_{lr} is reduced. As discussed above, this is because the atmospheric water path increases with a smaller γ_{lr}, which reduces T_{cnt}. The feedback of the H_2O continuum therefore has the opposite sign as the H_2O bands, in line with the analytical results. Finally, reducing the relative humidity increases T_{rad} in all regions dominated by water vapor, both in the H_2O bands below 600 cm^{-1}/above 1300 cm^{-1} and in the H_2O continuum around 1000 cm^{-1}, while the CO_2 band is unaffected.

Overall, Figure 4 underlines that comparatively simple physics is sufficient to explain the spectrally-resolved response of T_{rad} to different climate perturbations. To connect Figure 4 back to the total clear-sky longwave feedback we only need to consider how emission temperature changes play out once we average them into spectral bands, and how multiple bands add up to determine the net longwave feedback.

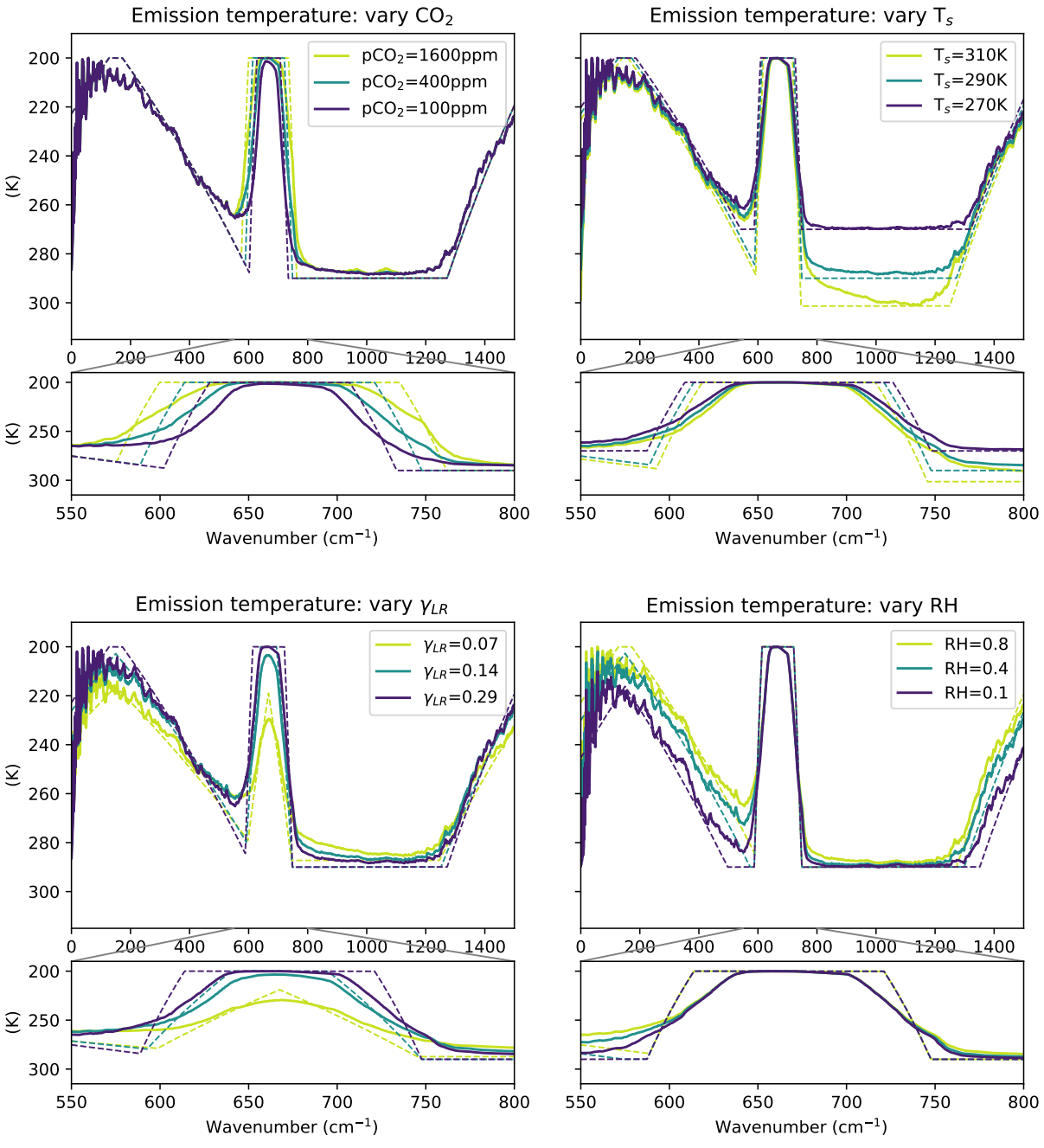

479 FIG. 4. Analytical emission temperatures (dashed), compared against numerical line-by-line results smoothed
480 with a median filter of width 50 cm^{-1}. Large rows show the entire infrared spectrum, small rows are zoomed
481 in on the CO_2 band. The y-axes are flipped so that emission temperature decreases going up, the same way
482 temperature decreases with altitude in Earth's atmosphere.

5. Analytical Feedbacks

Having derived expressions for the emission temperature in different parts of the LW spectrum, and verified these expressions against line-by-line calculations, we can now derive analytic expressions for the four spectral feedbacks: $\lambda_{\rm surf}$, $\lambda_{\rm co_2}$, $\lambda_{\rm H_2O}$ and $\lambda_{\rm cnt}$. Because each spectral feedback is defined as an integral over a relevant wavenumber range (Eqn. 16) we first need to estimate the width of different spectral bands.

a. Band widths

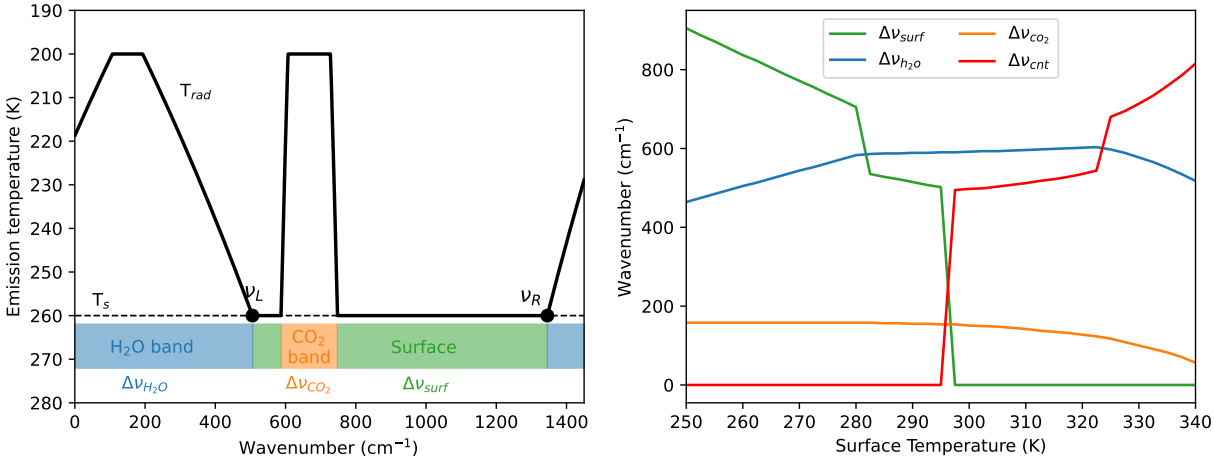

FIG. 5. Illustration of spectral band widths. The emission temperature is equal to the emission temperature of whichever emitter is coldest, $T_{\rm rad} = \min[T_{\rm co_2}, T_{\rm H_2O}, T_{\rm cnt}, T_s]$, or the stratospheric temperature. Left: Lines show the analytical $T_{\rm rad}$ (solid) and surface temperature T_s (dashed), while colored regions illustrate which emitters dominate in which band. The calculation shown uses T_s=260 K, RH = 0.8, and 400ppm of CO_2. Right: Band widths as a function of surface temperature, numerically calculated based on our emission temperature expressions. Here $\Delta\nu_{\rm H_2O}$ refers only to the rotational band at wavenumbers lower than 1000 cm^{-1}.

In line with the emission-level approximation and our results in Section 4, we define an absorption band as the spectral range in which a given absorber has the coldest emission temperature and therefore dominates the emission to space. For example, the CO_2 band covers all wavenumbers in which $T_{\rm co_2} < \min[T_{\rm H_2O}, T_{\rm cnt}, T_s]$, as illustrated in Figure 5. The width of the CO_2 band is then determined by the two wavenumbers ν^{edge} at which the emission temperature of CO_2 intersects the emission temperatures of its neighboring absorbers: $T_{\rm co_2}(\nu^{edge}) = \min[T_{\rm H_2O}(\nu^{edge}), T_{\rm cnt}, T_s]$.

1) CO_2 band width

To estimate the width of the CO_2 band we consider three situations: (1) the CO_2 concentration q_{co_2} is so low that even in the center of the CO_2 band the optical thickness is less than one; (2) a cold (or dry) atmosphere in which there is no overlap between the CO_2 and H_2O bands; and (3) a warm (or moist) atmosphere in which there is some overlap between CO_2 and H_2O.

First, at low CO_2 concentrations the band width of CO_2 is simply equal to zero. When does this situation occur? From the optical thickness of CO_2 (Eqn. 22), the column-integrated optical thickness in the middle of the CO_2 band is equal to $\tau_{co_2}(\nu_0, T_s) = q_{co_2}\tau^*_{co_2}(\nu_0)$ so

$$\Delta\nu_{co_2} = 0, \quad \text{if } q_{co_2}\tau^*_{co_2}(\nu_0) < 1. \tag{31}$$

Second, at non-negligible CO_2 concentration and cold surface temperatures, water vapor is a weak absorber and CO_2-H_2O overlap is negligible. In this case the edge of the CO_2 band can be defined as the wavenumber ν^{cold} at which T_{co_2} intersects with the surface temperature T_s, $T_{co_2}(\nu^{cold}) = T_s$. The emission temperature of CO_2 is equal to $T_{co_2} = T_s \times (\tau^*_{co_2} q_{co_2})^{-\gamma_{lr}/2}$ (Eqn. 25a), while our model of CO_2 spectroscopy states $\tau_{co_2}(\nu)^* \propto \exp(-|\nu - \nu_0|/l_\nu)$ (Eqn. 10). Combining the two equations yields

$$\nu^{cold} = \nu_0 \pm l_\nu \log\left(q_{co_2}\tau^*_{co_2}(\nu_0)\right). \tag{32}$$

Here $\tau^*_{co_2}(\nu_0) = \kappa_0(\nu_0)p_s/(2g)$ is the reference optical thickness in the center of the CO_2 band. The overall width of the CO_2 band at cold temperatures is therefore

$$\Delta\nu^{cold}_{co_2} = 2l_\nu \log\left(q_{co_2}\tau^*_{co_2}(\nu_0)\right). \tag{33}$$

To estimate the order of magnitude of $\Delta\nu^{cold}_{co_2}$ we use $\kappa_0 = 500$ m^2 kg^{-1} (from Section 2c) and a q_{co_2} that corresponds to 400ppm of CO_2. The optical thickness in the center of the CO_2 band is $\tau^*_{co_2}(\nu_0) \sim 1600$. This large optical thickness decreases exponentially with wavenumber away from ν_0, so that T_{co_2} equals T_s only ~ 80 cm^{-1} away from ν_0. Because CO_2's band shape is symmetric about ν_0, the present-day CO_2 band width is thus less than 200 cm^{-1}.

Third, at high temperatures the emission from the surface is replaced by H_2O emission, so $T_{co_2}(\nu^{hot}) = T_{H_2O}(\nu^{hot})$. Because the CO_2 band slope is much steeper than the H_2O band slope (see Fig. 3) we further approximate T_{H_2O} as constant across the CO_2 band and equal to its value in the CO_2 band center $T_{H_2O}(\nu) \approx T_{H_2O}(\nu_0)$. Combining the emission temperature of CO_2 (Eqn. 25a) with our model of CO_2 spectroscopy (Eqn. 10),

$$\nu^{hot} = \nu_0 \pm l_\nu \log\left[q_{co_2}\tau^*_{co_2}(\nu_0)\left(\frac{T_{H_2O}(\nu_0)}{T_s}\right)^{\frac{2}{\gamma_{lr}}}\right], \tag{34}$$

where the emission temperature of H_2O can be evaluated using Eqn. 25b. Physically speaking, the H_2O emission temperature is colder than the surface, $T_{H_2O}(\nu_0)/T_s < 1$, so our model correctly captures the fact that H_2O-CO_2 overlap decreases the width of the CO_2 band. Taking into account all three regimes, the overall width of the CO_2 band is therefore

$$\Delta\nu_{co_2} = \begin{cases} 0, & \text{if } q_{co_2}\tau^*_{co_2}(\nu_0) < 1 \\ 2\times\min\left(\nu^{hot}-\nu_0, \nu^{cold}-\nu_0\right), & \text{if } q_{co_2}\tau^*_{co_2}(\nu_0) \geq 1. \end{cases} \tag{35}$$

2) H_2O band width

To determine H_2O's band width the potential overlap with CO_2 matters less because (at present-day CO_2 concentrations) the CO_2 band is too narrow to block a significant portion of the emission by H_2O. However, at high temperatures competition between the H_2O bands and the H_2O continuum becomes important, so we again consider two temperature regimes. At cold temperatures continuum absorption is negligible and we solve $T_{H_2O}(\nu^{cold}) = T_s$. Combining the emission temperature of H_2O (Eqn. 25b) with our H_2O band model (Eqn. 11), this leads to

$$\nu_L^{cold} = \nu_{rot} + l_{rot}\log\left(\frac{\mathrm{RH}\tau^*_{rot}(\nu_{rot})}{1+\gamma_{wv}\gamma_{lr}}\left(\frac{T_s}{T_0}\right)^{\gamma_{wv}}\right), \tag{36a}$$

$$\nu_R^{cold} = \nu_{v-r} - l_{v-r}\log\left(\frac{\mathrm{RH}\tau^*_{v-r}(\nu_{v-r})}{1+\gamma_{wv}\gamma_{lr}}\left(\frac{T_s}{T_0}\right)^{\gamma_{wv}}\right), \tag{36b}$$

where ν_L is the left edge of the window below ~ 1000 cm^{-1}, and ν_R is the right edge of the window above ~ 1000 cm^{-1} (see Figure 5). The two H_2O bands have different spectral slopes, and subscript "rot" denotes quantities that are related to the rotational H_2O band at wavenumbers

below 1000 cm^{-1} while subscript "v-r" denotes quantities related to the vibrational-rotational H_2O band at wavenumbers above 1000 cm^{-1} (see Section 2). At high temperatures the continuum cuts off emission from the surface so the H_2O band edge ν^{hot} is determined by $T_{\mathrm{H_2O}}(\nu^{hot}) = T_{\mathrm{cnt}}$. Using the emission temperature of H_2O (Eqn. 25b) and our H_2O band model, we find

$$\nu_L^{hot} = \nu_{\mathrm{rot}} + l_{\mathrm{rot}} \log\left[\frac{\mathrm{RH}\tau^*_{\mathrm{rot}}(\nu_{\mathrm{rot}})}{1+\gamma_{\mathrm{wv}}\gamma_{\mathrm{lr}}}\left(\frac{T_0}{T_s}\right)^{1/\gamma_{\mathrm{lr}}}\left(\frac{T_{\mathrm{cnt}}}{T_0}\right)^{\frac{1+\gamma_{\mathrm{wv}}\gamma_{\mathrm{lr}}}{\gamma_{\mathrm{lr}}}}\right], \tag{37a}$$

$$\nu_R^{hot} = \nu_{\mathrm{v-r}} - l_{\mathrm{v-r}} \log\left[\frac{\mathrm{RH}\tau^*_{\mathrm{v-r}}(\nu_{\mathrm{v-r}})}{1+\gamma_{\mathrm{wv}}\gamma_{\mathrm{lr}}}\left(\frac{T_0}{T_s}\right)^{1/\gamma_{\mathrm{lr}}}\left(\frac{T_{\mathrm{cnt}}}{T_0}\right)^{\frac{1+\gamma_{\mathrm{wv}}\gamma_{\mathrm{lr}}}{\gamma_{\mathrm{lr}}}}\right], \tag{37b}$$

where the continuum emission temperature is given by Eqn. 25c. Combining both temperature regimes, the window width due to H_2O absorption is therefore

$$\begin{aligned}\Delta\nu_{\mathrm{surf}}(T_s, \mathrm{RH}, \gamma_{\mathrm{lr}}) &= \nu_R - \nu_L \\ &= \max(\nu_R^{cold}, \nu_R^{hot}) - \min(\nu_L^{cold}, \nu_L^{hot}).\end{aligned} \tag{38}$$

Similar to the CO_2 band width, Equations 36 and 37 become invalid at very low RH or T_s because in those situations H_2O ceases to be optically thick at all wavenumbers (mathematically, this happens when RH or T_s become small enough that the logarithms in Eqns. 36 and 37 change sign). We do not consider the limit $\mathrm{RH} \to 0$ in this paper, but care should be taken when applying our results to extremely dry or cold atmospheres.

Finally, our feedback expression for the H_2O feedback requires us to separately specify the width of the rotational H_2O band below 1000 cm^{-1}. This width can be estimated by assuming that the rotational band always extends from 0 cm^{-1} to the left edge of the window region ν_L (see Figure 5). Doing so presumes that H_2O is always optically thick at low wavenumbers around $\nu = 0$ cm^{-1}. While this assumption again breaks down in very cold or dry climates (the maximum absorption in the rotational band occurs around $\nu \sim 150$ cm^{-1}, not 0 cm^{-1}, so low wavenumbers could become optically thin even if the band center is still optically thick), in those climates the H_2O feedback becomes negligible anyway. The width of the rotational H_2O band is then

$$\Delta\nu_{\mathrm{H_2O}}(T_s, \mathrm{RH}, \gamma_{\mathrm{lr}}) \approx \nu_L - 0 = \min(\nu_L^{cold}, \nu_L^{hot}), \tag{39}$$

where the wavenumber ν_L denotes the left edge of the surface window (see above), as well as the right edge of the rotational H_2O band.

b. Surface Feedback

The surface feedback is given by

$$-\lambda_{\text{surf}} = \int_{\text{surf}} \pi \frac{dB_\nu}{dT}|_{T_s} e^{-\tau_{LW}} d\nu. \tag{40}$$

The column-integrated optical thickness at a single frequency is the sum over all absorbers at that frequency, $\tau_{LW}(\nu) = \tau_{H_2O}(\nu) + \tau_{co_2}(\nu) + \tau_{\text{cnt}}$. However, the optical thickness of H_2O and CO_2 drops off exponentially as a function of wavenumber away from their band centers. Thus most frequencies are either so optically thick with respect to H_2O and CO_2 that all surface radiation is absorbed by the atmosphere (and hence does not contribute to the surface feedback), or so optically thin that we can ignore H_2O and CO_2. Inside the window we therefore only consider absorption by the grey continuum, $\tau_{LW} \approx \tau_{\text{cnt}}$, while the H_2O and CO_2 bands primarily affect the surface feedback by setting the width of the window.

To determine the width of the window we first consider an atmosphere without CO_2. As discussed above, in this case the window region is set the H_2O bands, with ν_L denoting the left window edge around ~ 700 cm^{-1} and ν_R the right window edge around ~ 1200 cm^{-1}. The H_2O continuum is grey and so can be taken out of the spectral integral,

$$-\lambda_{\text{surf}} \approx e^{-\tau_{\text{cnt}}(T_s)} \int_{\nu_L}^{\nu_R} \pi \frac{dB_\nu}{dT}|_{T_s} d\nu.$$

We approximate the integral by treating the Planck function derivative as constant with respect to wavenumber, evaluated at the central wavenumber $\tilde{\nu}$ of the window region, so $\int dB_\nu/dT d\nu \propto dB_{\tilde{\nu}}/dT \times \Delta\nu$. In reality the Planck derivative is not constant with wavenumber, so our approximation should only be treated as a scaling which we account for by including a scaling constant c_{surf}. The magnitude of c_{surf} is further discussed below. The result is

$$-\lambda_{\text{surf}} \approx c_{\text{surf}} \times \pi \frac{dB_{\tilde{\nu}}}{dT}|_{T_s}\ e^{-\tau_{\text{cnt}}(T_s)}\ \Delta\nu_{\text{surf}},$$

where $\Delta\nu_{\rm surf} = \nu_R - \nu_L$ is the window region width due to H_2O line absorption (see Eqn. 38), and we determine the central wavenumber of the window as $\tilde{\nu} = (\nu_R + \nu_L)/2$.

Next, we add the effect of CO_2-surface spectral blocking. After all, even if the atmosphere contained no water vapor whatsoever, part of the surface's emission would still be absorbed by CO_2 and thus have no effect on the TOA feedback. We account for the potential overlap between the surface and CO_2 by simply subtracting the CO_2 band width from the H_2O-only window width,

$$\Delta\tilde{\nu}_{\rm surf} \quad = \quad \max\left[0, \Delta\nu_{\rm surf}(T_s, {\rm RH}, \gamma_{\rm lr}) - \Delta\nu_{\rm co_2}(q_{\rm co_2})\right], \tag{41}$$

where $\Delta\nu_{\rm co_2}$ is defined above (Eqn. 35) and the tilde distinguishes the window width here from the H_2O-only window width. Our final expression for the surface feedback is thus

$$-\lambda_{\rm surf} \quad \approx \quad c_{\rm surf} \times \pi \frac{dB_{\tilde{\nu}}}{dT}|_{T_s}\, e^{-\tau_{\rm cnt}(T_s)}\, \Delta\tilde{\nu}_{\rm surf}. \tag{42}$$

c. Non-Simpsonian H_2O feedback

The H_2O feedback is given by

$$-\lambda_{\rm H_2O} \quad = \quad \int_{\rm H_2O} \pi \frac{dB_\nu}{dT}|_{T_{\rm H_2O}} \frac{dT_{\rm H_2O}}{dTs} d\nu. \tag{43}$$

As sketched out in Figure 5, we consider the rotational H_2O band as ranging from $\nu \approx 0$ to the left edge of the window, ν_L. We do not consider the potential feedback from the vibration-rotation band at wavenumbers higher than ~ 1250 cm^{-1} and, for purposes of the H_2O feedback, also ignore CO_2-H_2O overlap effects.

The derivative of $T_{\rm H_2O}$ can be solved analytically. If water vapor behaved strictly according to Simpson's law then $dT_{\rm H_2O}/dT_s = 0$ and the H_2O feedback would be zero. Simpson's law is only

an approximation, however, so

$$\begin{aligned}\frac{dT_{\mathrm{H_2O}}}{dT_s} &= \frac{\partial T_{\mathrm{H_2O}}}{\partial T_s} + \frac{\partial T_{\mathrm{H_2O}}}{\partial \gamma_{\mathrm{lr}}}\frac{d\gamma_{\mathrm{lr}}}{dT_s} \\ &= \frac{1}{1+\gamma_{\mathrm{wv}}\gamma_{\mathrm{lr}}}\frac{T_{\mathrm{H_2O}}}{T_s} + \\ &\quad \frac{\gamma_{\mathrm{wv}}\gamma_{\mathrm{lr}} - \gamma_{\mathrm{wv}}\log\left(\frac{T_s}{T_0}\right) + \log\left(\frac{1+\gamma_{\mathrm{wv}}\gamma_{\mathrm{lr}}}{\mathrm{RH}\tau_0^*}\right)}{(1+\gamma_{\mathrm{wv}}\gamma_{\mathrm{lr}})^2} T_{\mathrm{H_2O}} \times \frac{d\gamma_{\mathrm{lr}}}{dT_s}. \end{aligned} \tag{44}$$

One could also explicitly write out the lapse rate derivative $d\gamma_{\mathrm{lr}}/dT_s$, but the resulting expressions are long and do not lead to additional physical insight, so in practice we evaluate $d\gamma_{\mathrm{lr}}/dT_s$ numerically. To estimate a typical value for $dT_{\mathrm{H_2O}}/dT_s$ we ignore lapse rate changes, that is, the second term in Equation 44. Assuming values representative of Earth's tropics, $1+\gamma_{\mathrm{wv}}\gamma_{\mathrm{lr}} = 1+1/7\times 20 \sim 4$, and representative temperatures $T_{\mathrm{H_2O}} \sim 240$ K (see Figure 4) and $T_s \sim 300$ K, a characteristic value for $dT_{\mathrm{H_2O}}/dT_s$ is thus

$$\frac{dT_{\mathrm{H_2O}}}{dT_s} \sim \frac{1}{4}\times\frac{240}{300} = \frac{1}{5}, \tag{45}$$

in line with the numerical results of Jeevanjee et al. (2021a).

Next, we treat the H_2O feedback similar to the surface feedback. We assume the integrand of the spectral feedback integral is approximately constant with respect to wavenumber, and equal to its value at a central frequency $\tilde{\nu}$. The feedback is then

$$\begin{aligned}-\lambda_{\mathrm{H_2O}} &= \int_0^{\nu_L} \pi \frac{dB_\nu}{dT}|_{T_{\mathrm{H_2O}}} \frac{dT_{\mathrm{H_2O}}}{dTs} d\nu \\ &\approx c_{\mathrm{H_2O}} \times \pi \left.\frac{dB_{\tilde{\nu}}}{dT}\right|_{T_{\mathrm{H_2O}}(\tilde{\nu})} \times \left.\frac{dT_{\mathrm{H_2O}}}{dTs}\right|_{\tilde{\nu}} \times \Delta\nu_{\mathrm{H_2O}}, \end{aligned} \tag{46}$$

where $\Delta\nu_{\mathrm{H_2O}} = \nu_L$ is the width of the H_2O band, $\tilde{\nu} = \nu_L/2$ is the central wavenumber of the H_2O band, and $c_{\mathrm{H_2O}}$ is again a scaling constant to account for the fact that we are replacing a spectral integral with simple multiplication.

d. H_2O continuum feedback

The H_2O continuum feedback is

$$-\lambda_{\rm cnt} = \int_{\rm cnt} \pi \frac{dB_\nu}{dT}|_{T_{\rm cnt}} \frac{dT_{\rm cnt}}{dT_s} d\nu. \tag{47}$$

We apply the same logic as for the surface and H_2O feedbacks. The derivative $dT_{\rm cnt}/dT_s$ can be solved for analytically: because $T_{\rm cnt}$ has no direct dependence on T_s, we have

$$\begin{aligned} \frac{dT_{\rm cnt}}{dT_s} &= \frac{\partial T_{\rm cnt}}{\partial \gamma_{\rm lr}} \frac{d\gamma_{\rm lr}}{dT_s} \\ &= \frac{T_{\rm cnt}}{\gamma_{\rm lr}(2\gamma_{\rm wv} - a)} \frac{d\gamma_{\rm lr}}{dT_s}. \end{aligned} \tag{48}$$

One important difference between the continuum and the other feedbacks is that the continuum is transparent across all wavenumbers at low surface temperatures, and only becomes optically thick at high surface temperatures. We approximate the continuum's emissivity as $1 - e^{-\tau_{\rm cnt}}$, which correctly captures the limiting behavior of an emitter at small and large optical thickness ($\tau_{\rm cnt} \ll 1$ versus $\tau_{\rm cnt} \gg 1$). The continuum can only dominate the atmosphere's emission at wavenumbers at which CO_2 and H_2O absorption is weak, so we set the effective width of the continuum equal to the width of the window region $\Delta\tilde{\nu}_{\rm surf}$, defined above. The continuum feedback is then

$$\begin{aligned} -\lambda_{\rm cnt} &= \int_{\rm cnt} \pi \frac{dB_\nu}{dT}|_{T_{\rm cnt}} \frac{dT_{\rm cnt}}{dT_s} d\nu \\ &\approx c_{\rm cnt} \times \pi \frac{dB_{\tilde{\nu}}}{dT}|_{T_{\rm cnt}} \times \frac{dT_{\rm cnt}}{dT_s} \times \Delta\tilde{\nu}_{\rm surf}(1 - e^{-\tau_{\rm cnt}}) \end{aligned} \tag{49}$$

where $c_{\rm cnt}$ is again a scaling constant. The sign of $\lambda_{\rm cnt}$ is positive because the bulk lapse rate decreases with warming, $d\gamma_{\rm lr}/dT_s < 0$. As discussed above, this means the H_2O continuum acts as a positive/destabilizing feedback and has the opposite sign of the negative/stabilizing H_2O feedback.

e. CO_2 radiator fin feedback

For the CO_2 feedback we introduce an idealized "ditch" model, as shown in Figure 6. Our approach is closely related to the CO_2 forcing models of Wilson and Gea-Banacloche (2012) and

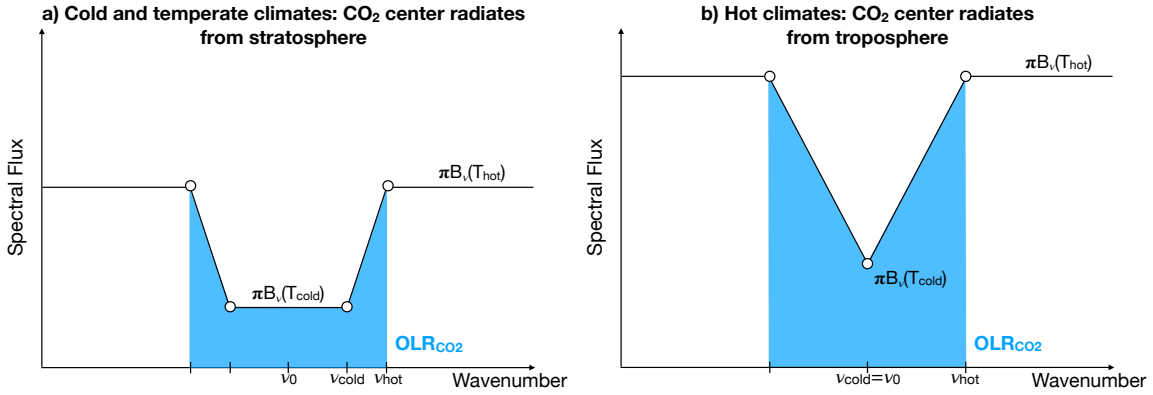

654 FIG. 6. A CO_2 "ditch" model: the CO_2 band emits $\pi B_\nu(T_{\rm cold})$ in its center, its flanks emit $\pi B_\nu(T_{\rm hot})$, and the
655 slopes in-between are approximated as linear and symmetric. Shaded blue area is the OLR contribution from the
656 CO_2 band. Left: in cold climates or at high CO_2 abundances the CO_2 band center radiates from the stratosphere.
657 Right: in hot climates or at low CO_2 abundances the CO_2 band center radiates from the troposphere.

660 Jeevanjee et al. (2021b) – in Appendix A we show that this ditch model also be used to rederive the
661 results of those previous studies, underlining the close relationship between forcing and feedbacks.

662 We approximate the CO_2 band as symmetric around the central frequency $\nu_0 = 667$ cm^{-1}. The
663 center of the band emits $\pi B_\nu(T_{\rm cold})$ while outside the band the emission is $\pi B_\nu(T_{\rm hot})$. Here $T_{\rm cold}$
664 and $T_{\rm hot}$ are cold and hot emission temperatures, while $\nu_{\rm hot}$ and $\nu_{\rm cold}$ denote the edges of the CO_2
665 ditch. At low and moderate surface temperatures the CO_2 band center around 667 cm^{-1} radiates
666 from the stratosphere, so $T_{\rm cold}$ is equal to the stratospheric temperature. However, this situation is
667 no longer true at high surface temperatures. Physically, the tropopause rises as the surface warms.
668 If we warm the surface while holding CO_2 concentration fixed (this is implicit in the feedback
669 definition, which is the change in OLR per change in surface temperature while keeping CO_2
670 fixed), more parts of the CO_2 band that were previously in the stratosphere have to start radiating
671 from the troposphere. Eventually, even the CO_2 band center radiates from the troposphere so the
672 rectangular CO_2 ditch turns into a triangle (see Fig. 6b). Here we leave our expressions general to
673 allow for either situation.

674 The CO_2 band is relatively narrow, so we can neglect the wavenumber dependence of the Planck
675 function and evaluate it at the center of the CO_2 band, $\pi B_\nu(T) \approx \pi B_{\nu_0}(T)$. Treating the slopes of
676 the CO_2 ditch as piecewise-linear, the OLR from the CO_2 band is then simply the area of the ditch

shape in Figure 6a,

$$\begin{aligned}\mathrm{OLR}_{\mathrm{co_2}} &= 2\int_{\nu_0}^{\nu_{\mathrm{hot}}} \pi B_{\nu_0}(T_{\mathrm{co_2}})d\nu \\ &= \left[\pi B_{\nu_0}(T_{\mathrm{hot}}) + \pi B_{\nu_0}(T_{\mathrm{cold}})\right](\nu_{\mathrm{hot}} - \nu_{\mathrm{cold}}) + 2\pi B_{\nu_0}(T_{\mathrm{cold}})(\nu_{\mathrm{cold}} - \nu_0). \end{aligned} \quad (50)$$

It follows that the OLR change in response to some climate perturbation is

$$\begin{aligned}\Delta\mathrm{OLR}_{\mathrm{co_2}} &= \mathrm{OLR}'_{\mathrm{co_2}} - \mathrm{OLR}_{\mathrm{co_2}} \\ &= \left[\pi B_{\nu_0}(T'_{\mathrm{hot}}) + \pi B_{\nu_0}(T'_{\mathrm{cold}})\right](\nu'_{\mathrm{hot}} - \nu'_{\mathrm{cold}}) - \left[\pi B_{\nu_0}(T_{\mathrm{hot}}) + \pi B_{\nu_0}(T_{\mathrm{cold}})\right](\nu_{\mathrm{hot}} - \nu_{\mathrm{cold}}) + \\ &\quad 2\pi B_{\nu_0}(T'_{\mathrm{cold}})(\nu'_{\mathrm{cold}} - \nu_0) - 2\pi B_{\nu_0}(T_{\mathrm{cold}})(\nu_{\mathrm{cold}} - \nu_0), \end{aligned} \quad (51)$$

where primes indicate perturbed variables. For the CO_2 feedback the relevant perturbation is a change in surface temperature ΔT_s, while for the forcing the relevant perturbation is a change in $q_{\mathrm{co_2}}$ (see Appendix A). If ΔT_s is small enough we can series expand and drop higher-order terms. For example, the perturbation of the emission at the CO_2 band edge is

$$\pi B_{\nu_0}(T'_{\mathrm{hot}}) = \pi B_{\nu_0}(T_{\mathrm{hot}}) + \pi \frac{dB_{\nu_0}}{dT}|_{T_{\mathrm{hot}}} \frac{dT_{\mathrm{hot}}}{dT_s}\Delta T_s,$$

with similar expressions for T'_{cold}, ν'_{cold}, and ν'_{cold}. Plugging back into Equation 51, the feedback of the CO_2 ditch is

$$\begin{aligned}-\lambda_{\mathrm{co_2}} &= \lim_{\Delta T_s \to 0} \frac{\Delta\mathrm{OLR}_{\mathrm{co_2}}}{\Delta T_s} \\ &= \left[\pi \frac{dB_{\nu_0}}{dT}\bigg|_{T_{\mathrm{hot}}} \frac{dT_{\mathrm{hot}}}{dT_s} + \pi \frac{dB_{\nu_0}}{dT}\bigg|_{T_{\mathrm{cold}}} \frac{dT_{\mathrm{cold}}}{dT_s}\right](\nu_{\mathrm{hot}} - \nu_{\mathrm{cold}}) \\ &\quad + \left[\pi B_{\nu_0}(T_{\mathrm{hot}}) + \pi B_{\nu_0}(T_{\mathrm{cold}})\right]\left(\frac{d\nu_{\mathrm{hot}}}{dT_s} - \frac{d\nu_{\mathrm{cold}}}{dT_s}\right) \\ &\quad + 2\,\pi \frac{dB_{\nu_0}}{dT}\bigg|_{T_{\mathrm{cold}}} \frac{dT_{\mathrm{cold}}}{dT_s}(\nu_{\mathrm{cold}} - \nu_0) + 2B_{\nu_0}(T_{\mathrm{cold}})\frac{d\nu_{\mathrm{cold}}}{dT_s}. \end{aligned} \quad (52)$$

Equation 52 gives the most general expression for the feedback of the CO_2 ditch. To evaluate this expression we need to specify how the emission temperatures T_{hot}, T_{cold} and the CO_2 band edges ν_{hot}, ν_{cold} vary as a function of surface temperature.

At cold surface temperatures we again ignore H_2O absorption around the CO_2 band so $T_{\rm hot} = T_s$. Similarly, the tropopause is low and the CO_2 band center radiates from the stratosphere, so $T_{\rm cold} = T_{strat}$ and $dT_{\rm cold}/dT_s = 0$. As in Section 5a, we find the band edges $\nu_{\rm hot}$ and $\nu_{\rm cold}$ by solving $T_{\rm co_2}(\nu_{\rm hot}) = T_s$ and $T_{\rm co_2}(\nu_{\rm cold}) = T_{strat}$. The results are $\nu_{\rm hot} = \nu_0 + l_\nu \log[\tau^*_{\rm co_2}(\nu_0) q_{\rm co_2}]$, and $\nu_{\rm cold} = \nu_0 + l_\nu \log[\tau^*_{\rm co_2}(\nu_0) q_{\rm co_2} (T_{strat}/T_s)^{2/\gamma_{\rm lr}}]$. We can see that the hot CO_2 band edge does not change under surface warming, $d\nu_{\rm hot}/dT_s = 0$, while the sensitivity of the cold or stratospheric band edge to surface warming is

$$\begin{aligned} \frac{d\nu_{\rm cold}}{dT_s} &= \left.\frac{\partial \nu_{\rm cold}}{\partial T_s}\right|_{\gamma_{\rm lr}} + \left.\frac{\partial \nu_{\rm cold}}{\partial \gamma_{\rm lr}}\right|_{T_s} \frac{d\gamma_{\rm lr}}{dT_s} \\ &= -\frac{2 l_\nu}{\gamma_{\rm lr} T_s} + \frac{2 l_\nu}{\gamma_{\rm lr}^2} \log\left(\frac{T_s}{T_{strat}}\right) \frac{d\gamma_{\rm lr}}{dT_s}. \end{aligned} \tag{53}$$

The lapse rate change $d\gamma_{\rm lr}/dT_s$ is always negative, so if we warm the surface while holding CO_2 concentration fixed the portion of the CO_2 band inside the stratosphere shrinks, $d\nu_{\rm cold}/dT_s < 0$. This is again a simple consequence of a rising tropopause. As the surface warms, the tropopause moves to lower pressures, thus moving more of CO_2's emission from the stratosphere into the tropopause. Plugging back into Equation 52, the CO_2 feedback at cold surface temperatures is

$$-\lambda^{cool}_{\rm co_2} = \pi \left.\frac{dB_{\nu_0}}{dT}\right|_{T_s} \frac{2}{\gamma_{\rm lr}} \log\left(\frac{T_s}{T_{strat}}\right) + \left[\pi B_{\nu_0}(T_s) - \pi B_{\nu_0}(T_{strat})\right] \times \left(\frac{2 l_\nu}{\gamma_{\rm lr} T_s} - \frac{2 l_\nu}{\gamma_{\rm lr}^2} \log\left(\frac{T_s}{T_{strat}}\right) \frac{d\gamma_{\rm lr}}{dT_s}\right) \tag{54}$$

At high surface temperatures the CO_2 band center moves into the tropopause and the rectangular ditch turns into a triangle (see lower left in Fig. 4, and sketch in Fig. 6b). We set $\nu_{\rm cold} = \nu_0$, where the central wavenumber ν_0 is set by the spectroscopic properties of CO_2 and so is fixed under surface warming ($d\nu_{\rm cold}/dT_s = 0$). The emission temperature in the center of the CO_2 band is now $T_{\rm cold} = T_{\rm co_2}(\nu_0)$, where $T_{\rm co_2}$ is the emission temperature of CO_2 (Eqn. 25a). The crucial difference between high and low surface temperatures is that once the CO_2 band center moves into the tropopause $T_{\rm cold}$ is no longer constant,

$$\begin{aligned} \frac{dT_{\rm co_2}(\nu_0)}{dT_s} &= \left.\frac{\partial T_{\rm co_2}(\nu_0)}{\partial T_s}\right|_{\gamma_{\rm lr}} + \left.\frac{\partial T_{\rm co_2}(\nu_0)}{\partial \gamma_{\rm lr}}\right|_{T_s} \frac{d\gamma_{\rm lr}}{dT_s} \\ &= \frac{T_{\rm co_2}(\nu_0)}{T_s} - \frac{T_{\rm co_2}(\nu_0)}{2} \log[q_{\rm co_2} \tau^*_{\rm co_2}(\nu_0)] \, \frac{d\gamma_{\rm lr}}{dT_s}. \end{aligned} \tag{55}$$

The outer edges of the CO_2 band at high temperatures are set by water vapor absorption, $T_{\rm hot} = \min[T_{H_2O}(\nu_0), T_{\rm cnt}]$. We treat H_2O as Simpsonian, so $dT_{\rm hot}/dT_s \approx 0$, and also ignore non-Simpsonian shifts in the outer CO_2 band edge, $d\nu_{\rm hot}/dT_s \approx 0$. Plugging back into Equation 52, the feedback at high surface temperatures is then

$$\begin{aligned} -\lambda_{\rm co_2}^{hot} &= \pi \left.\frac{dB_{\nu_0}}{dT}\right|_{T_{\rm cold}} \frac{dT_{\rm cold}}{dT_s}(\nu_{\rm hot} - \nu_{\rm cold}) \\ &= \pi \left.\frac{dB_{\nu_0}}{dT}\right|_{T_{\rm cold}} \frac{dT_{\rm cold}}{dT_s}\, l_\nu \log\left[\tau^*_{\rm co_2}(\nu_0) q_{\rm co_2} \left(\frac{T_{\rm hot}}{T_s}\right)^{\frac{2}{\gamma_{\rm lr}}}\right]. \end{aligned} \tag{56}$$

Finally, when does the CO_2 band center change from a stratospheric radiator at low T_s to a tropospheric radiator at high T_s, which also determines the transition between $\lambda_{\rm co_2}^{cool}$ and $\lambda_{\rm co_2}^{hot}$? Based on line-by-line calculations with 400 ppm of CO_2, Appendix B shows that the smoothed emission temperature in the CO_2 band center moves out of the stratosphere at surface temperatures above 310 K. We therefore identify 310 K as the transition point between the low-temperature and high-temperature CO_2 feedback regimes. Note, however, that this value also depends on CO_2 concentration.

Multiplying the low-temperature regime with a scaling constant $c_{\rm co_2}$, similar to our other spectral feedbacks, the overall CO_2 radiator fin feedback is thus

$$\lambda_{\rm co_2} = \begin{cases} c_{\rm co_2} \times \lambda_{\rm co_2}^{cool} & \text{if } T_s \leq 310 \text{ K} \\ \lambda_{\rm co_2}^{hot} + b & \text{if } T_s > 310 \text{ K}. \end{cases} \tag{57}$$

where we choose the constant b to ensure that $\lambda_{\rm co_2}$ remains continuous at 310 K (in practice b is always of order unity, $b \sim 0.5$).

f. Validation against LBL calculations

To test our analytical feedback expressions we again use 1D calculations with PyRADS. One potential issue is that our derivations use the bulk lapse rate approximation, and so might differ from realistic feedbacks. Appendix C compares feedbacks calculated with a moist adiabat to feedbacks with bulk lapse rate profiles. Overall, the bulk lapse rate approximation only introduces minor errors in λ_{LW} over the temperature range $250 - 320$ K, while errors in individual spectral

feedbacks as well as in λ_{LW} become notable at $\sim$ 320 K. We therefore consider the bulk lapse rate approximation sufficiently accurate below 320 K, but care should be taken when applying our analytical expressions to extremely hot climates. To better match the derivations, the PyRADS calculations here also use vertical profiles with a bulk lapse rate, so $T = T_s(p/p_s)^{\gamma_{\rm lr}}$. We explore the surface temperature-dependence of spectral feedbacks at high and low relative humidity (RH=0.8 and RH=0.1), without CO_2 and with 400 ppm of CO_2, for four sets of calculations total.

To compare our analytical expressions against the 1D calculations we need to specify the scaling constants $c_{\rm surf}$, $c_{\rm H_2O}$, $c_{\rm cnt}$, and $c_{\rm co_2}$. We pick these constants to match the 1D calculations at RH=0.8 and 400 ppm of CO_2. The temperature-dependence varies significantly between different feedbacks, so we choose $c_{\rm surf}$ to match $\lambda_{\rm surf}$ at low temperatures (T_s = 250 K), $c_{\rm cnt}$ to match $\lambda_{\rm cnt}$ at high temperatures (T_s = 330 K), and $c_{\rm H_2O}$ and $c_{\rm co_2}$ to match $\lambda_{\rm H_2O}$ and $\lambda_{\rm co_2}$ around Earth's present-day mean temperature (T_s = 290 K). Table 1 shows the resulting values. In this Section we choose the scaling constants to match the 1D calculations with bulk lapse rates. We note that Section 6 considers a feedback calculation specifically for present-day Earth, so in that Section we use slightly-different scaling constants which match 1D calculations with moist adiabatic lapse rates (see Appendix C). Regardless of the exact values, however, the scaling constants are always of order unity.

Figure 7 shows that our analytical expressions successfully capture the basic state-dependence of λ_{LW} as well as of its spectral constituents. The longwave feedback λ_{LW} is sensitive to changes in surface temperature, but it also varies in response to humidity and CO_2 changes. Comparing between different panels in Figure 7, λ_{LW} becomes larger with decreasing relative humidity (also see McKim et al. 2021). In contrast, CO_2 evens out the temperature-dependence of λ_{LW}, by decreasing λ_{LW} at cold temperatures and increasing λ_{LW} at high temperatures. Importantly, the analytical expressions capture most of the variation in λ_{LW} and recover the state-dependence of the net longwave feedback.

To understand the overall behavior of λ_{LW} we turn to the individual spectral feedbacks. The surface feedback $\lambda_{\rm surf}$ is generally the dominant term in the spectral decomposition. Without CO_2, $\lambda_{\rm surf}$ makes up at least 90% of λ_{LW} below 300 K. The presence of CO_2 decreases $\lambda_{\rm surf}$ but even in this case $\lambda_{\rm surf}$ makes up at least 60% of λ_{LW} below 300 K. Our analytical expressions thus agree with previous studies which argued that Earth's longwave feedback is dominated by the

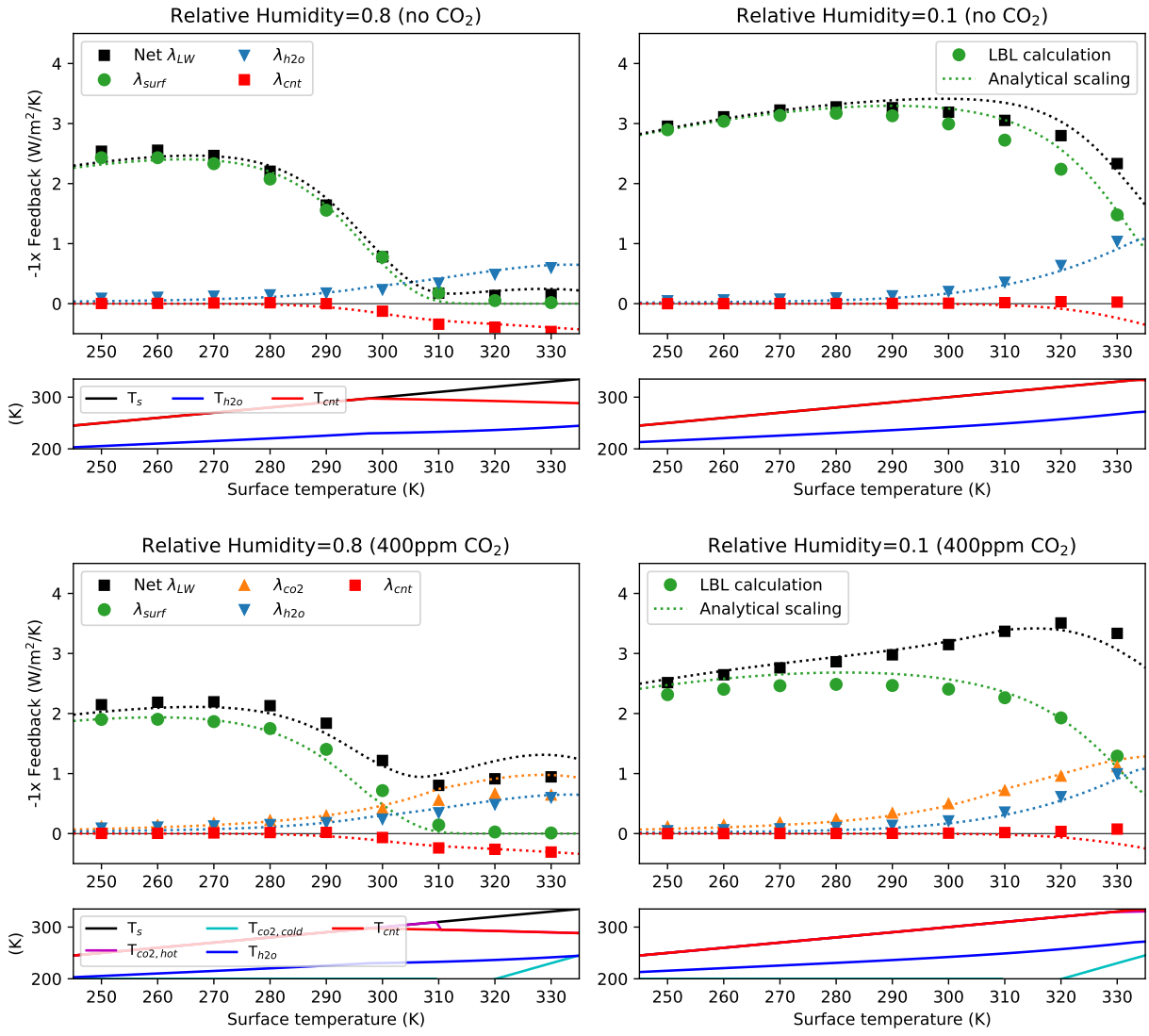

FIG. 7. Spectral feedbacks calculated using a bulk lapse rate (symbols), compared against the analytical scalings (lines). Top row shows calculations without CO_2, bottom row 400ppm of CO_2. The large panels show feedbacks while small panels show the corresponding analytical emission temperatures.

surface feedback (Koll and Cronin 2018; Raghuraman et al. 2019). This situation changes at high temperatures, however, once the surface window closes, at which point λ_{LW} becomes dominated by atmospheric feedbacks.

Next, in line with Section 4, the CO_2 radiator fin feedback acts to stabilize Earth's climate , and its importance increases with surface temperature. Below 300 K, $\lambda_{\mathrm{co_2}}$ contributes less than 20% of the total feedback. However, $\lambda_{\mathrm{co_2}}$ rapidly grows with surface temperature such that at 330 K and

TABLE 2. Summary of main theoretical results.

Emission temperatures

$$T_{co_2}(\nu) = T_s \left(\frac{1}{\tau^*_{co_2}(\nu) q_{co_2}} \right)^{\gamma_{lr}/2}$$

$$T_{H_2O}(\nu) = T_0 \left(\frac{1+\gamma_{wv}\gamma_{lr}}{\tau^*_{H_2O}(\nu) RH} \right)^{\frac{\gamma_{lr}}{1+\gamma_{wv}\gamma lr}} \left(\frac{T_s}{T_0} \right)^{\frac{1}{1+\gamma_{wv}\gamma lr}}$$

$$T_{cnt} = T_0 \left(\frac{(2\gamma_{wv}-a)\gamma_{lr}}{\tau^*_{cnt} RH^2} \right)^{\frac{1}{2\gamma_{wv}-a}}$$

Feedbacks

$$-\lambda_{surf} = c_{surf} \times \pi \frac{dB_{\tilde{\nu}}}{dT}|_{T_s} \Delta\tilde{\nu}_{surf} e^{-\tau_{cnt}}$$

$$-\lambda_{H_2O} = c_{H_2O} \times \pi \left. \frac{dB_{\tilde{\nu}}}{dT} \right|_{T_{H_2O}(\tilde{\nu})} \times \frac{dT_{H_2O}(\tilde{\nu})}{dT_s} \times \Delta\nu_{H_2O}$$

$$-\lambda_{cnt} = c_{cnt} \times \pi \left. \frac{dB_{\nu}}{dT} \right|_{\tilde{\nu}, T_{cnt}} \times \frac{dT_{cnt}}{dT_s} \times \Delta\tilde{\nu}_{surf} \left(1 - e^{-\tau_{cnt}}\right)$$

$$-\lambda_{co_2} = \begin{cases} c_{co_2} \times \frac{2\pi}{\gamma_{lr}} \left. \frac{dB_{\nu_0}}{dT} \right|_{T_s} \log\left(\frac{T_s}{T_{strat}} \right) - \left[\pi B_{\nu_0}(T_s) - \pi B_{\nu_0}(T_{strat}) \right] \times \frac{d\nu_{cold}}{dT_s} & \text{at low } T_s \\ \pi \left. \frac{dB_{\nu_0}}{dT} \right|_{T_{cold}} \frac{dT_{cold}}{dT_s} (\nu_{hot} - \nu_{cold}) + b & \text{at high } T_s \end{cases}$$

high relative humidity λ_{co_2} makes up almost 70% of λ_{LW}. Interestingly, if RH is high, λ_{co_2} becomes equal to λ_{surf} at surface temperatures around ~ 305 K. Extrapolating from these 1D calculations to Earth's spatial feedback pattern, we can expect that Earth's feedback is dominated by the surface in most regions, but that atmospheric feedbacks become important in the inner tropics – an issue we explore in detail in Section 6.

Finally, again in line with our analytical results, the two water vapor feedbacks λ_{H_2O} and λ_{cnt} have opposing signs. At high relative humidity λ_{H_2O} and λ_{cnt} partially cancel. In contrast, at low relative humidity λ_{cnt} becomes negligible while λ_{H_2O} only changes moderately – a non-Simpsonian effect. The different sensitivity to RH arises because the continuum's optical thickness scales as $\tau_{cnt} \propto RH^2$, whereas the optical thickness in the water vapor bands only scales as $\tau_{H_2O} \propto RH$. Decreases in relative humidity therefore increase λ_{LW} both by increasing the surface feedback λ_{surf} and by reducing λ_{cnt}, so that H_2O acts as a net stabilizing feedback. Comparing λ_{H_2O} and λ_{co_2} at present-day CO_2 levels, we see that the two feedbacks are roughly equal in magnitude. Non-Simpsonian H_2O effects are thus about as important as the CO_2 radiator fin for Earth's current longwave feedback.

6. The spatial pattern of λ_{LW}

In the previous two sections we found that our analytical model, summarized in Table 2, successfully captures the behavior of Earth's emission temperature T_{rad} as well as the state-dependence of λ_{LW}. In this section we perform another validation by reproducing the spatial map of λ_{LW} for Earth's present-day climate. First, we generate a reference map of λ_{LW} using the radiative kernel technique (Soden et al. 2008), which diagnoses λ_{LW} by combining a radiative kernel with the forced response from climate model output. Here these quantities are evaluated using preindustrial and 4xCO_2 simulations from the HadGEM2 climate model (Collins et al. 2011), described below. Next, we generate maps of λ_{LW} using our analytical expressions and variable amounts of input data from HadGEM2. We find that the spatial pattern of λ_{LW} can be largely constrained using only knowledge about the preindustrial climate, that is, without any knowledge of the climate's forced response. As a best estimate of Earth's true clear-sky longwave feedback we therefore also generate a map of λ_{LW} using only our analytical expressions and the observationally-constrained ERA5 reanalysis dataset (Hersbach et al. 2020).

a. Description of Kernel and Input Data

We follow established methods for the kernel calculation. We use the HadGEM2 radiative kernel and, for consistency with the analytical model (which assumes the stratosphere is isothermal and at a fixed temperature), we set the kernel to zero inside the stratosphere. The tropopause is defined as in Soden et al. (2008): the tropopause pressure p_{tp} linearly increases with latitude, from 100hPa at the equator to 300hPa at the poles. The analytical model also assumes relative humidity stays fixed under surface warming, so we do not include relative humidity changes in the kernel calculation. Doing so is justified because RH feedbacks only make a minor contribution to λ_{LW} in individual climate models, and the RH feedback moreover tends to cancel in the multi-model mean (Zelinka et al. 2020). To compute the forced response we use HadGEM2 climatologies from the CMIP5 archive for a preindustrial control simulation and an abrupt-4XCO2 simulation. By multiplying the kernel with the forced response one obtains a map of the change in top-of-atmosphere (TOA) radiation (Soden et al. 2008). To compute a feedback one additionally needs to normalize the change in TOA radiation by a change in temperature. Consistent with our derivations we compute local-local feedback maps, that is, we divide the local change in OLR deduced from the kernel by

the local change in surface temperature (Feldl and Roe 2013; Armour et al. 2013; Bloch-Johnson et al. 2020).

We compare the spatial map of λ_{LW} from the kernel against maps of λ_{LW} from our analytical expressions. The analytical expressions require six input parameters: CO_2 abundance, surface temperature T_s, stratosphere temperature T_{strat}, relative humidity RH, temperature lapse rate $\gamma_{\rm lr}$, and the change in lapse rate under surface warming $d\gamma_{\rm lr}/dT_s$. Except for the lapse rate change $d\gamma_{\rm lr}/dT_s$, all these inputs can be obtained from a single climate state (e.g., the HadGEM2 preindustrial state) and do not require any knowledge of the climate's forced response. CO_2 is set to be spatially uniform at 400 ppm (results are highly similar if using a preindustrial 285 ppm instead); the surface temperature T_s is taken as the air temperature at 2m; and the stratospheric temperature T_{strat} is set equal to the temperature at the tropopause pressure level, $T_{strat} = T(p_{\rm tp})$, using the above tropopause definition of Soden et al. (2008). The relative humidity RH is set equal to the column relative humidity, defined as the ratio between the atmospheric column's water vapor path and its water vapor path at saturation (e.g., Bretherton et al. 2005),

$$\mathrm{RH} = \frac{\mathrm{WVP}}{\mathrm{WVP}^*}, \tag{58}$$

$$= \frac{\int_{p_{\rm tp}}^{p_s} q\ dp/g}{\int_{p_{\rm tp}}^{p_s} q^*\ dp/g}. \tag{59}$$

Here the vertical integral is taken from the tropopause $p_{\rm tp}$ down to the surface to exclude the strongly sub-saturated stratosphere. One could in principle also approximate RH using other measures of atmospheric humidity; however, the column relative humidity is a natural choice because it correctly captures the atmosphere's total water vapor path, which in turn determines the width of the window region and $\lambda_{\rm surf}$.

Next, the lapse rate $\gamma_{lr} = d\ln T/d\ln p$ varies strongly in the vertical. We compute the mean lapse rate using a mass-weighted vertical average,

$$\gamma_{\rm lr} = \frac{1}{p_1 - p_{\rm tp}} \int_{p_{\rm tp}}^{p_1} \frac{p}{T}\frac{dT}{dp} dp, \tag{60}$$

where the average is taken from the tropopause level $p_{\rm tp}$ down to $p_1 = 850$ hPa. We exclude the stratosphere and near-surface layers to avoid inversions (our derivations break down if $\gamma_{\rm lr} < 0$).

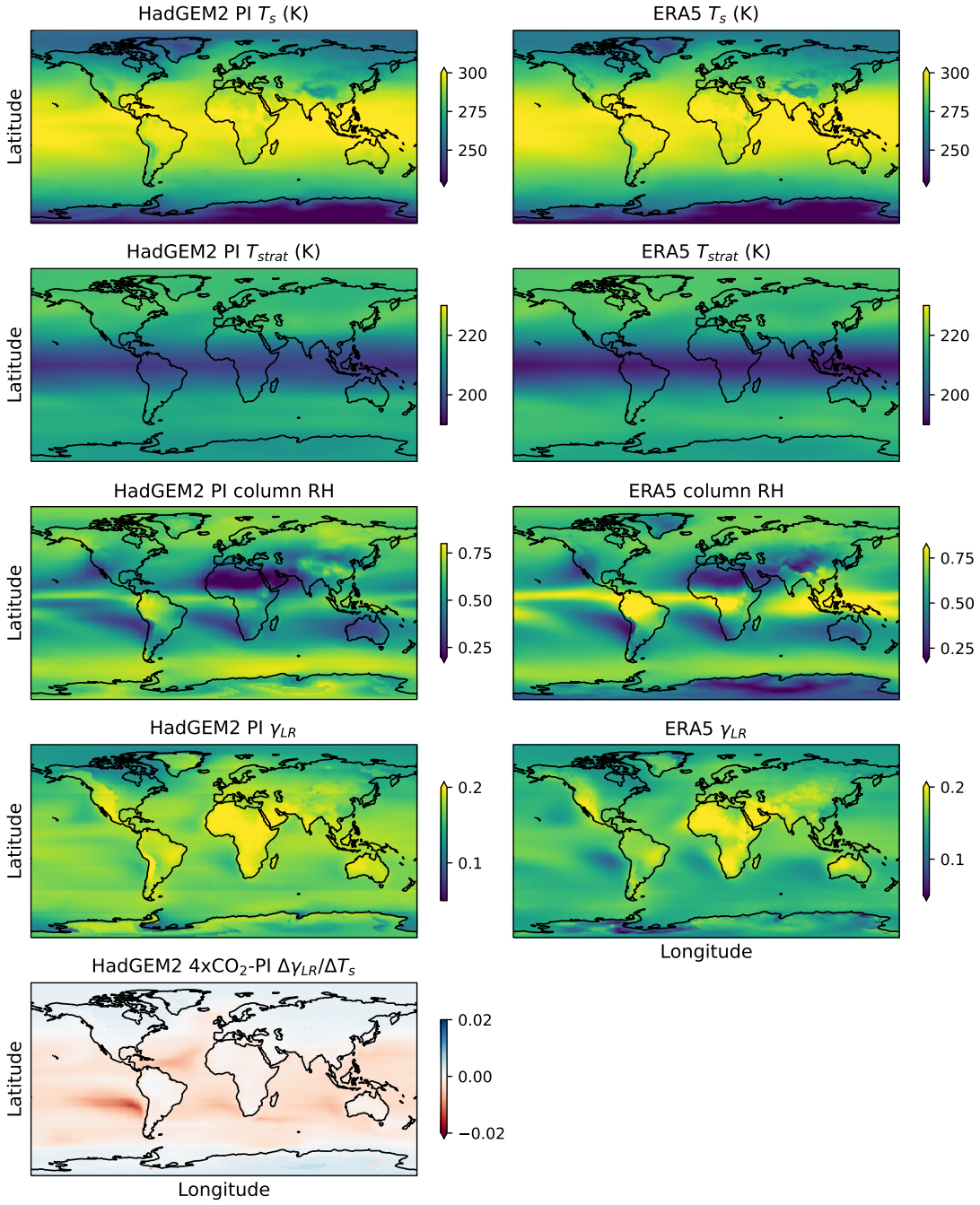

FIG. 8. Input data used to evaluate the analytical feedback model. Left column: input from the HadGEM2 GCM. The top four panels are from a preindustrial (PI) simulation, the bottom panel shows the lapse rate difference $\Delta\gamma_{\rm lr}/\Delta T_s$ between 4xCO$_2$ and PI simulations. Right column: input from ERA5 reanalysis averaged over the years 1980-1999.

One could also evaluate γ_{lr} using Equation 5 and an appropriate tropopause definition; however, this approach makes the inferred lapse rates highly sensitive to the specific tropopause definition, which we side-step by using Equation 60 instead.

Finally, the only input in our analytical expressions that requires information about the climate's forced response is the change in lapse rate $d\gamma_{\mathrm{lr}}/dT_s$. We use two different approaches. First, we compute $d\gamma_{\mathrm{lr}}/dT_s$ as the change in γ_{lr} between abrupt-4x and preindustrial HadGEM2 simulations. As in feedback calculations that are based on radiative kernels (e.g., Soden et al. 2008), this approach is purely diagnostic, since one can only deduce λ_{LW} when the climate's forced response is already known. We also demonstrate a second approach in which we do not use any information about the climate's forced response. To do so we assume $d\gamma_{\mathrm{lr}}/dT_s$ is locally moist-adiabatic, i.e., we compute $d\gamma_{\mathrm{lr}}/dT_s$ using a bulk lapse rate evaluated at the local surface temperature. Doing so is only an approximation, but it has the advantage that it allows one to predict λ_{LW} solely using information about a climate's current state (preindustrial climate model data or reanalysis data of present-day Earth).

Figure 8 shows the input data maps used to evaluate the analytical expressions. The left column is based on the HadGEM2 simulations, the right column is based on the ERA5 reanalysis data. Spatial variations are most notable in the maps of surface temperature T_s, column relative humidity RH, and mean lapse rate γ_{lr}, which show qualitatively (if not necessarily quantitatively) similar patterns between HadGEM2 and ERA5. In contrast, apart from minor midlatitude stationary wave patterns, the stratospheric temperature T_{strat} is fairly symmetric zonally and varies by only about 20 K between the equator and poles. The lapse rate change under surface warming, $\Delta\gamma_{\mathrm{lr}}/\Delta T_s$, requires us to know a climate's forced response and so is only shown for HadGEM2. In agreement with previous studies, $\Delta\gamma_{\mathrm{lr}}/\Delta T_s$ exhibits an equator-pole contrast – at low latitudes γ_{lr} decreases, as expected for a moist adiabat, while at high latitudes γ_{lr} increases under global warming (e.g., Payne et al. 2015; Cronin and Jansen 2016; Stuecker et al. 2018).

b. Model validation: Kernel versus analytical feedback maps

The maps of λ_{LW} resulting from the kernel and analytical calculations are shown in Figure 9. The kernel-derived map of λ_{LW} shows strong spatial contrasts between high latitudes, subtropics, and inner tropics (Fig. 9, top left). The longwave feedback is smallest in the inner tropics, especially

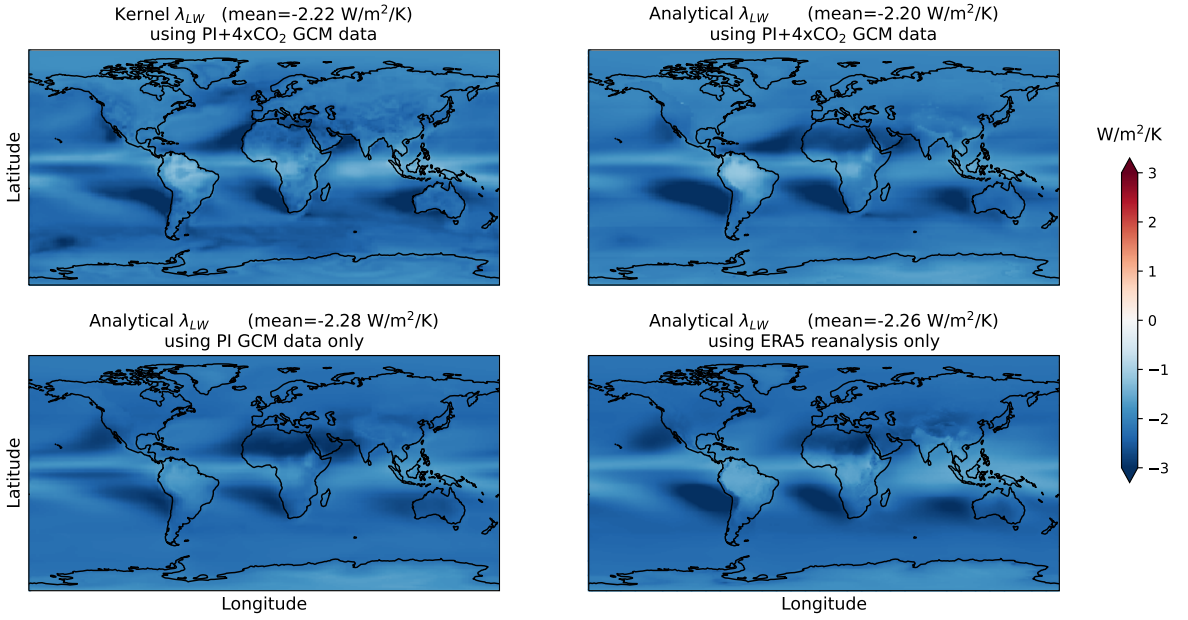

FIG. 9. Spatial pattern of λ_{LW} deduced from varying amounts of input data. Top left: Reference. Computed using a radiative kernel, plus preindustrial (PI) and abrupt-4x CO_2 GCM simulations. Top right: from our analytical expressions, plus PI and 4xCO_2 GCM data. Bottom left: from our analytical expressions and PI GCM data only. Bottom right: from our analytical expressions and ERA5 reanalysis data only. Means shown above each subpanel are area-weighted global means, and do not take into account the pattern of warming.

in the intertropical convergence zone (ITCZ), while it is largest in the subtropics, especially in subtropical deserts like the Sahara and over eastern ocean basins. At mid and high latitudes the magnitude of λ_{LW} is close to the global mean. Zonal contrasts are largest in the subtropics and more muted at higher latitudes.

Importantly, all analytical calculations recover the same spatial patterns as the radiative kernel: λ_{LW} approaches zero in the ITCZ, is largest in the subtropics, and intermediate at high latitudes. Comparing the global area-weighted means of λ_{LW}, we find that the analytical expressions also get the mean feedback magnitude right. The mean of λ_{LW} is -2.2 W m^{-2} K^{-1} in the kernel-derived map, while it varies between -2.2 and -2.3 W m^{-2} K^{-1} in the analytical maps. Note that to compute the true global-mean λ_{LW}, the local feedback maps in Figure 9 should be weighted by the pattern of the forced surface temperature response (Feldl and Roe 2013; Armour et al. 2013). Doing so is ambiguous when the forced response is not known, however, so we compare area-weighted means instead.

The agreement between kernel and analytical feedbacks in Figure 9 is less good at regional scales. For example, even the analytical calculation that uses both preindustrial (PI) and 4xCO_2 HadGEM2 data, and thus should agree most closely with the kernel, shows noticeable deviations from the kernel map over the Sahara and over the Eastern Pacific off the coast of Peru. Similarly, the kernel-derived map of λ_{LW} shows clear small-scale variation over extratropical oceans, in particular over the Southern Ocean and North Atlantic, while all analytical maps show little-to-no variation in these regions.

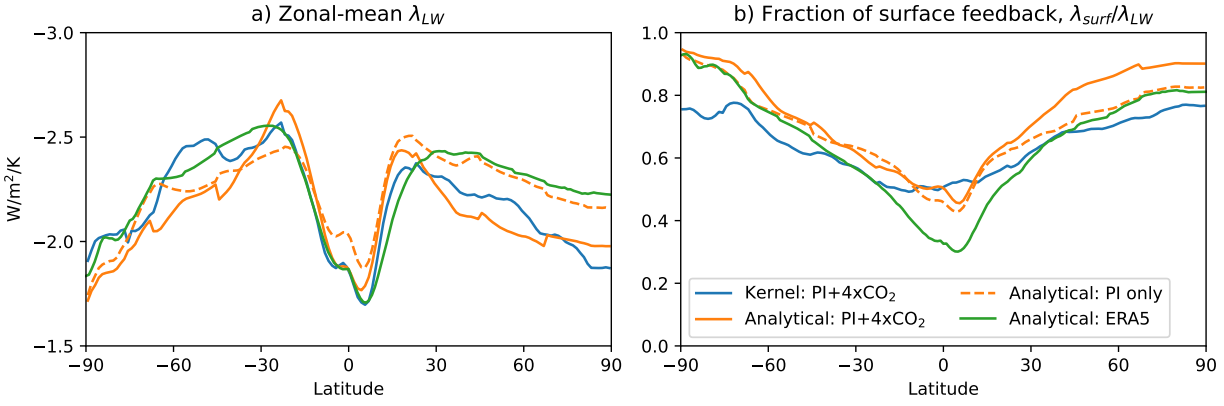

FIG. 10. a) Zonal mean of the λ_{LW} maps in Figure 9. b) Zonal mean fraction of the surface feedback to the net feedback, $\lambda_{\text{surf}}/\lambda_{LW}$.

To further analyze the match between kernel and analytical feedbacks, Figure 10 shows the zonal means of λ_{LW} and the fraction of λ_{LW} that is due to the surface feedback λ_{surf}. Kernel and analytical calculations agree well in the ITCZ but less so at high latitudes, with differences in the zonal-mean λ_{LW} reaching up to 10% over the Arctic. Similarly, the analytical calculations qualitatively recover the partition between surface and atmospheric feedbacks (panel b) but deviate at regional scales. In the HadGEM2 kernel $\lambda_{\text{surf}}/\lambda_{LW}$ is about 60% in the tropics and about 80% at the poles, which is comparable to the value of 60% reported by Raghuraman et al. (2019). In contrast, our analytical model tends to modestly over-predict the surface feedback, with $\lambda_{\text{surf}}/\lambda_{LW}$ varying from about 60% in the tropics to over 90% at the poles. One plausible reason for the deviations in $\lambda_{\text{surf}}/\lambda_{LW}$ is that our expressions do not consider ozone. Ozone absorbs effectively inside the window region, which should reduce the window width $\Delta\nu_{surf}$ and thus also the surface feedback λ_{surf}. Nevertheless, both kernel and analytical calculations agree that λ_{LW} is dominated by λ_{surf} across most of the

globe, while atmospheric feedbacks only start to rival λ_{surf} in the inner tropics and particularly inside the ITCZ.

Despite some noticeable inaccuracies at regional scales, we conclude that the analytical expressions are sufficiently accurate to be useful for understanding the spatial pattern of λ_{LW}. To do so we break λ_{LW} up into its spectral constituents next.

c. Spectral decomposition

Figure 11 shows the spectral decomposition of our analytical feedback maps. In agreement with Section 5, where we found that λ_{LW} is dominated by λ_{surf} across a wide surface temperature range, the spatial variation in λ_{LW} is also largely dominated by the spatial variation in λ_{surf}. The surface feedback is large at high latitudes, peaks in the subtropics, and decreases to less than a fourth of its peak value in the ITCZ. This contrasts with what one might naively expect for a blackbody: if the atmosphere was completely transparent the surface feedback would simply be $4\sigma T_s^3$ so one might expect that λ_{surf} is smallest at high latitudes and largest at the equator (also see Henry and Merlis 2019). In reality λ_{surf} does increase with surface temperature, $\lambda_{\text{surf}} \propto \pi B_\nu(T_s)$, but it also rapidly decreases with increasing relative humidity due to the closing of the window and the onset of the continuum, $\lambda_{\text{surf}} \propto \Delta\nu_{\text{surf}} \exp(-\tau_{\text{cnt}})$.

In contrast to the surface, atmospheric feedbacks are small at the poles and large in the tropics. This is partly because atmospheric feedbacks are sensitive to both γ_{lr} and $d\gamma_{\text{lr}}/dT_s$, largely via the change in emission temperatures $dT_{\text{H}_2\text{O}}/dT_s$ and dT_{co_2}/dT_s, whereas the surface feedback only depends on γ_{lr}, via the influence of the lapse rate on the column water vapor path which in turn sets the window width $\Delta\nu_{\text{surf}}$ (see Table 2). Since $d\gamma_{\text{lr}}/dT_s$ has a distinct equator-pole gradient (Fig. 8), the spatial pattern of lapse-rate changes thus helps create a pole-equator contrast in atmospheric feedbacks. In agreement with Section 5, where we found that λ_{co_2} and $\lambda_{\text{H}_2\text{O}}$ are quite similar in magnitude, the maps of λ_{co_2} and $\lambda_{\text{H}_2\text{O}}$ are also highly similar and the global mean values are within 10% in all cases. This is a coincidence caused by Earth's present-day CO_2 concentration, and may not be the case in other climates (e.g., for paleoclimates).

We further analyze the spectral feedback maps in Figure 11 by computing their spatial correlation with the inputs in Figure 8. For simplicity we only discuss correlations here based on ERA5, but similar correlations also hold in HadGEM data. In the tropics (equatorward of 30 degrees) λ_{surf}

is strongly correlated with RH, with a correlation coefficient $r = 0.95$. Note the sign of the correlation – larger values of RH coincide with a larger (i.e., less negative) λ_{surf}. In contrast, the net atmospheric feedback $\lambda_{\text{co}_2} + \lambda_{\text{H}_2\text{O}} + \lambda_{\text{cnt}}$ is strongly correlated with the lapse rate γ_{lr}, $r = 0.83$. Here the sign of the correlation is again positive, such that a smaller lapse rate coincides with a more negative atmospheric feedback. These correlations are much more significant than any intrinsic correlations in the input data. For example, in the tropics the column relative humidity is essentially independent of γ_{lr} ($r = 0.14$) and only weakly correlated with surface temperature ($r = 0.43$). The surface feedback is therefore most sensitive to the closing of the window region, which in the tropics is dominated by the spatial pattern of RH, while the atmospheric feedback primarily responds to the atmospheric lapse rate $\gamma_{\text{lr}}(T_s)$ and, if known, its change under warming $d\gamma_{\text{lr}}/dT_s$. The varying sensitivity to RH versus γ_{lr} is reflected in the individual feedback maps. For example, λ_{surf} is large both over the Sahara and over the Eastern Pacific close to the coast of Peru because both regions are extremely dry (see Fig. 8). In contrast, λ_{co_2} and $\lambda_{\text{H}_2\text{O}}$ are relatively small over the Sahara but large over the Eastern Pacific, due to the fact that γ_{lr} is large over the Sahara but small over the Eastern Pacific.

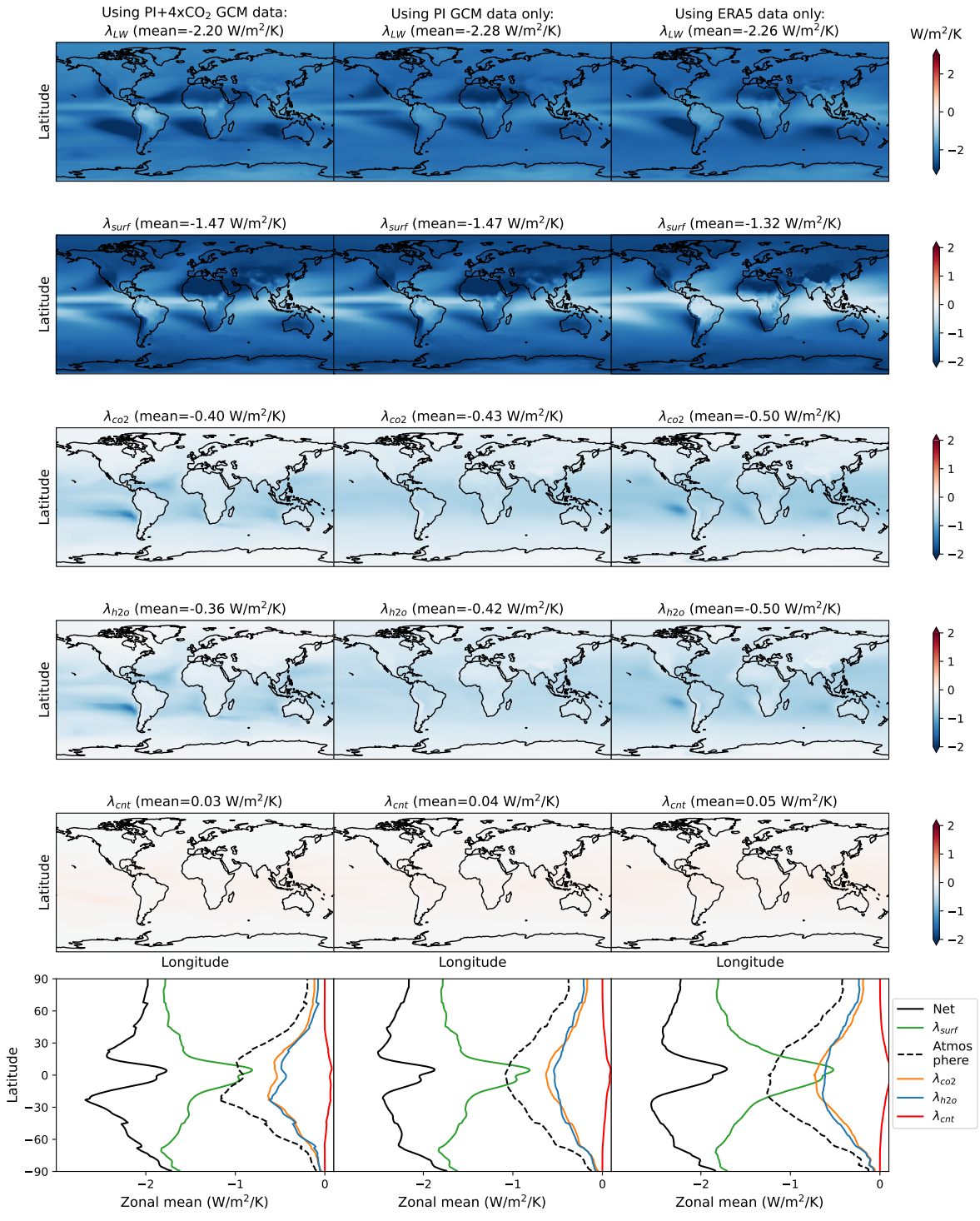

912 FIG. 11. Net feedback λ_{LW} and its spectral components. Left column: calculation based on input data from
913 preindustrial (PI) and 4xCO_2 GCM simulations. Middle column: calculation only using preindustrial (PI) GCM
914 input data. Right column: calculation only using ERA5 reanalysis input data. Note the different color axes
915 between different rows. Bottom row shows zonal means of the overlying rows.

7. Discussion & Conclusions

In this paper, we have presented a novel decomposition of Earth's clear-sky longwave feedback λ_{LW} into four spectral components: a surface Planck feedback (λ_{surf}), a CO_2 "radiator fin" feedback (λ_{co_2}), a non-Simpsonian water vapor band feedback ($\lambda_{\text{H}_2\text{O}}$), and a destabilizing water vapor continuum feedback (λ_{cnt}). We have derived simple analytic expressions for each of these spectral feedbacks, which accurately reproduce the results of line-by-line calculations and can also be used to diagnose the local feedback map of climate models. In fact, we have been able to predict Earth's spatial feedback map solely using reanalysis data. This requires assuming lapse rate changes are moist adiabatic, but our analysis suggests that even with this approximation one can obtain a reasonable estimate. In order to fully predict Earth's true global-mean λ_{LW} the spatial feedback maps derived from our expressions must be weighted by the equilibrium spatial pattern of warming, which is not known for Earth's present climate. Nevertheless, we have shown that from a radiative perspective the factors determining λ_{LW} can all be understood from first principles, adding further support to the close agreement for λ_{LW} between observations and climate models.

The picture of Earth's clear-sky longwave feedback that emerges from this perspective is relatively simple, consisting of a surface feedback plus atmospheric feedbacks from CO_2 and H_2O. At present the surface feedback λ_{surf} is the most important contributor in the global-mean and at most latitudes, with its relative importance determined by the distribution of atmospheric water vapor. λ_{surf} is largest in the dry subtropics, consistent with the view that these are the locus of Earth's stabilizing longwave feedback (Pierrehumbert 1995; McKim et al. 2021), and smallest in the deep tropics, where the surface's emission is blocked by the H_2O continuum. The CO_2 and H_2O feedbacks λ_{co_2} and $\lambda_{\text{H}_2\text{O}}$ play a supporting role to λ_{surf} at mid and high latitudes, but they dominate Earth's feedback in the deep tropics. The H_2O continuum provides a negligible feedback at present, but the continuum itself is still important through its influence on λ_{surf}.

This picture is arguably a more intuitive starting point for reasoning about different climates than the traditional decomposition of λ_{LW} into Planck, Lapse Rate and Water Vapor feedbacks. As discussed by Cronin and Dutta (in revision at QJRMS), it is already non-trivial to accurately estimate the supposedly-simple Planck feedback from first principles. Similarly, one can qualitatively reason that Lapse Rate and Water Vapor feedbacks both increase in magnitude under global warming, but these are large and of opposite sign, so it is difficult to predict their net change and, by extension,

the T_s-dependence of λ_{LW}, in the traditional decomposition without resorting to numerical models. The strong cancellations between Planck, Lapse Rate and Water Vapor feedbacks can be alleviated by considering traditional feedbacks in a fixed relative humidity framework (Ingram 2010; Held and Shell 2012), but this comes at the cost that the state-dependence of the Planck feedback is no longer trivial to understand at fixed RH.

In contrast, the state-dependence of λ_{LW} is fairly straightforward to understand from a spectral perspective, at least in broad brushstrokes. For present-day Earth the T_s-dependence of λ_{LW} is dominated by the surface in most regions. If relative humidity is fixed, λ_{surf} increases at very cold temperatures, peaks around $260-290$ K depending on RH, and then decreases again (see Section 5). The decrease is rapid at high RH due to the H_2O continuum, but much slower at low RH. Atmospheric feedbacks also have state-dependence. All of them increase in magnitude as the atmosphere warms, and are further amplified by a weakening lapse rate. In the tropics the state-dependence of λ_{LW} is thus set by the interplay between a decreasing surface feedback and increasing atmospheric feedbacks. This can lead to surprising dynamics – at high RH, λ_{surf} decreases more rapidly with warming than λ_{co_2} and $\lambda_{\text{H}_2\text{O}}$ increase. As a result λ_{LW} becomes non-monotonic with warming and develops a local minimum around ~ 310 K, which leads to a local maximum in climate sensitivity (Seeley and Jeevanjee 2021).

The state-dependence of λ_{LW} at temperatures far above ~ 310 K is beyond the scope of this paper, but a spectral perspective points to the importance of stabilizing H_2O and CO_2 bands versus the destabilizing H_2O continuum as Earth approaches the runaway greenhouse. The main caveat here is that Earth's net feedback does not necessarily stay dominated by λ_{LW} at very high surface temperatures, while atmospheric feedbacks also become more complicated at high temperatures due to effects such as non-dilute thermodynamics and surface pressure changes (Goldblatt et al. 2013; Ramirez et al. 2014).

There are several remaining shortcomings in our analysis of λ_{LW} that are beyond the scope of this paper. Perhaps the largest is our assumption of an atmosphere that is approximately moist adiabatic, such that temperature has to monotonically decrease with altitude. In the real world inversions are common, particularly in polar regions and over subtropical oceans. Comparable to the long-standing discussion about how to interpret the Lapse Rate feedback at high latitudes in the traditional decomposition (e.g., Cai and Lu 2009; Payne et al. 2015; Stuecker et al. 2018; Boeke

et al. 2021), we therefore expect that our approach here only provides a first stab at understanding the processes which shape λ_{LW} in inversion regions.

Another assumption is that we ignore stratospheric changes, even though stratospheric cooling induced by rising CO_2 levels is a major and robust signal of anthropogenic warming (e.g., Vallis et al. 2014). It is notable that the radiative changes due to stratospheric cooling are also hard to intuitively explain using traditional feedbacks. Climate model analyses typically treat the stratosphere's fast radiative adjustment to CO_2 changes as a process distinct from Planck, Lapse Rate, and Water Vapor feedbacks. Our derivations here sidestep this issue and treat T_{strat} as a fixed parameter.

Similarly, our derivations ignore the potential feedback from relative humidity changes. In reality there is no guarantee that relative humidity changes will remain negligible under global warming, let alone that they can be neglected when trying to understand paleoclimates. In principle our analysis starting from the emission level approximation can be extended to estimate the feedbacks associated with changes in either RH or T_{strat}; RH changes would lead to a feedback term proportional to $\partial T_{\text{rad}}/\partial \text{RH}$, while stratospheric changes would lead to a feedback term proportional to $\partial T_{\text{rad}}/\partial T_{strat}$. We hope to explore the consequences of such changes in future work.

Acknowledgments. D.D.B.K. thanks Jeevanjee Gardens in Nairobi. N.J.L. was supported by the NOAA Climate Program Office's Modeling, Analysis, Predictions, and Projections program through grant NA20OAR4310387.

Data availability statement. HadGEM2 GCM data is publicly available in CMIP data archives. The HadGEM2 radiative kernel is available at `https://archive.researchdata.leeds.ac.uk/382`. ERA5 reanalysis data are available from the Copernicus Climate Change Service. Scripts to compute our analytical feedbacks will be posted online once the manuscript is accepted for publication.

APPENDIX A

CO_2 Forcing

The CO_2 ditch model can be used to explain the CO_2 forcing in addition to the CO_2 radiator fin feedback. This section rederives the CO_2 forcing expressions from Wilson and Gea-Banacloche

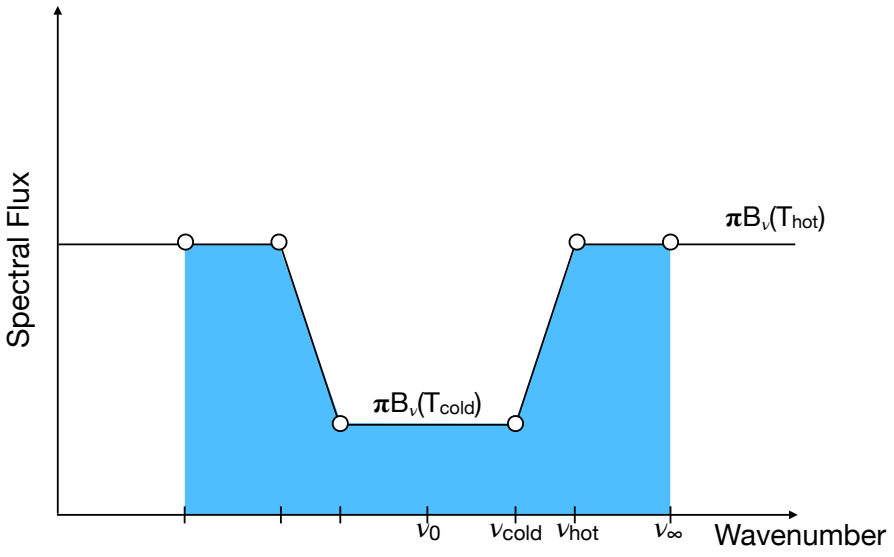

FIG. A1. CO_2 ditch model for the CO_2 forcing. The shaded blue area is the OLR contribution from the CO_2 band as well as neighboring spectral regions. The band edges $\nu_{\rm hot}$ and $\nu_{\rm cold}$ vary in response to CO_2 concentration $q_{\rm co_2}$, while ν_∞ is sufficiently far away from the CO_2 band to be constant with respect to $q_{\rm co_2}$.

(2012) and Jeevanjee et al. (2021b), which are valid as long as the CO_2 band center radiates from the stratosphere. Note that our CO_2 feedback model only considers OLR changes inside the CO_2 band (see Figure 6). This is because the effect of CO_2 on $\lambda_{\rm H_2O}$ or $\lambda_{\rm surf}$ is separately considered in the derivation of those feedbacks. Forcing is defined as the OLR change integrated across all wavenumbers, however, so here we need to consider the expanded shaded region shown in Figure A1. The OLR integrated across this expanded region, $\rm OLR_+$, is

$$\begin{aligned} \mathrm{OLR}_+ &= 2\int_{\nu_0}^{\nu_{\nu_\infty}} \pi B_{\nu_0}(T_{\rm rad})\,d\nu \\ &= \left[\pi B_{\nu_0}(T_{\rm hot}) + \pi B_{\nu_0}(T_{\rm cold})\right](\nu_{\rm hot} - \nu_{\rm cold}) + 2\pi B_{\nu_0}(T_{\rm cold})(\nu_{\rm cold} - \nu_0) + \\ &\quad 2\pi B_{\nu_0}(T_{\rm hot})(\nu_\infty - \nu_{\rm hot}). \end{aligned} \tag{A1}$$

The forcing from a doubling of CO_2 is then

$$\begin{aligned} F^{2x}_{\mathrm{co_2}} &= -\frac{d\mathrm{OLR}_+}{d\log_2(q_{\mathrm{co_2}})} \\ &= -\ln(2)\frac{d\mathrm{OLR}_+}{d\ln q_{\mathrm{co_2}}} \\ &= -\ln(2)\left(\left[\pi B_{\nu_0}(T_{\mathrm{hot}})+\pi B_{\nu_0}(T_{\mathrm{cold}})\right]\left(\frac{d\nu_{\mathrm{hot}}}{d\ln q_{\mathrm{co_2}}}-\frac{d\nu_{\mathrm{cold}}}{d\ln q_{\mathrm{co_2}}}\right)+2\pi B_{\nu_0}(T_{\mathrm{cold}})\frac{d\nu_{\mathrm{cold}}}{d\ln q_{\mathrm{co_2}}}- \right. \\ &\quad \left. 2\pi B_{\nu_0}(T_{\mathrm{hot}})\frac{d\nu_{\mathrm{hot}}}{d\ln q_{\mathrm{co_2}}}\right) \end{aligned} \tag{A2}$$

The minus sign in the first line ensures that forcing is positive when OLR decreases, while the base-2 logarithm is necessary because forcing is defined with respect to a CO_2 doubling. In the second step we then change the logarithm's base to the natural logarithm, while in the third step we treat the emission temperatures T_{hot} and T_{cold} as constant. This is valid because the derivative of OLR with respect to $q_{\mathrm{co_2}}$ is taken at fixed T_s (i.e., at fixed surface temperature, the temperature outside the CO_2 band and in the stratosphere are both independent of CO_2 concentration).

The CO_2 band edges are defined by $T_{\mathrm{co_2}}(\nu_{\mathrm{hot}}) = T_{hot}$ and $T_{\mathrm{co_2}}(\mathrm{cold}) = T_{strat}$. Solving for ν_{hot} and ν_{cold} we find

$$\nu_{\mathrm{hot}} = \nu_0 + l_\nu \log\left[q_{\mathrm{co_2}}\tau^*_{\mathrm{co_2}}(\nu_0)\left(\frac{T_{\mathrm{hot}}}{T_s}\right)^{2/\gamma_{\mathrm{lr}}}\right] \tag{A3}$$

$$\nu_{\mathrm{cold}} = \nu_0 + l_\nu \log\left[q_{\mathrm{co_2}}\tau^*_{\mathrm{co_2}}(\nu_0)\left(\frac{T_{strat}}{T_s}\right)^{2/\gamma_{\mathrm{lr}}}\right]. \tag{A4}$$

We can see that the CO_2 band edges shift equally in response to a CO_2 increase:

$$\frac{d\nu_{\mathrm{hot}}}{d\ln q_{\mathrm{co_2}}} = \frac{d\nu_{\mathrm{cold}}}{d\ln q_{\mathrm{co_2}}} = l_\nu. \tag{A5}$$

It follows that the first term proportional to $d\nu_{\mathrm{hot}}/d\ln q_{\mathrm{co_2}} - d\nu_{\mathrm{cold}}/d\ln q_{\mathrm{co_2}}$ in Equation A2 is zero. The CO_2 forcing is thus

$$F^{2x}_{\mathrm{co_2}} = 2\ln(2) l_\nu \left(\pi B_{\nu_0}(T_{\mathrm{hot}}) - \pi B_{\nu_0}(T_{\mathrm{cold}})\right), \tag{A6}$$

which is identical to the analytical CO_2 forcing model in Jeevanjee et al. (2021b) (their Equations 7 and 14).

APPENDIX B

Transition from stratospheric to tropospheric CO_2 radiator fin

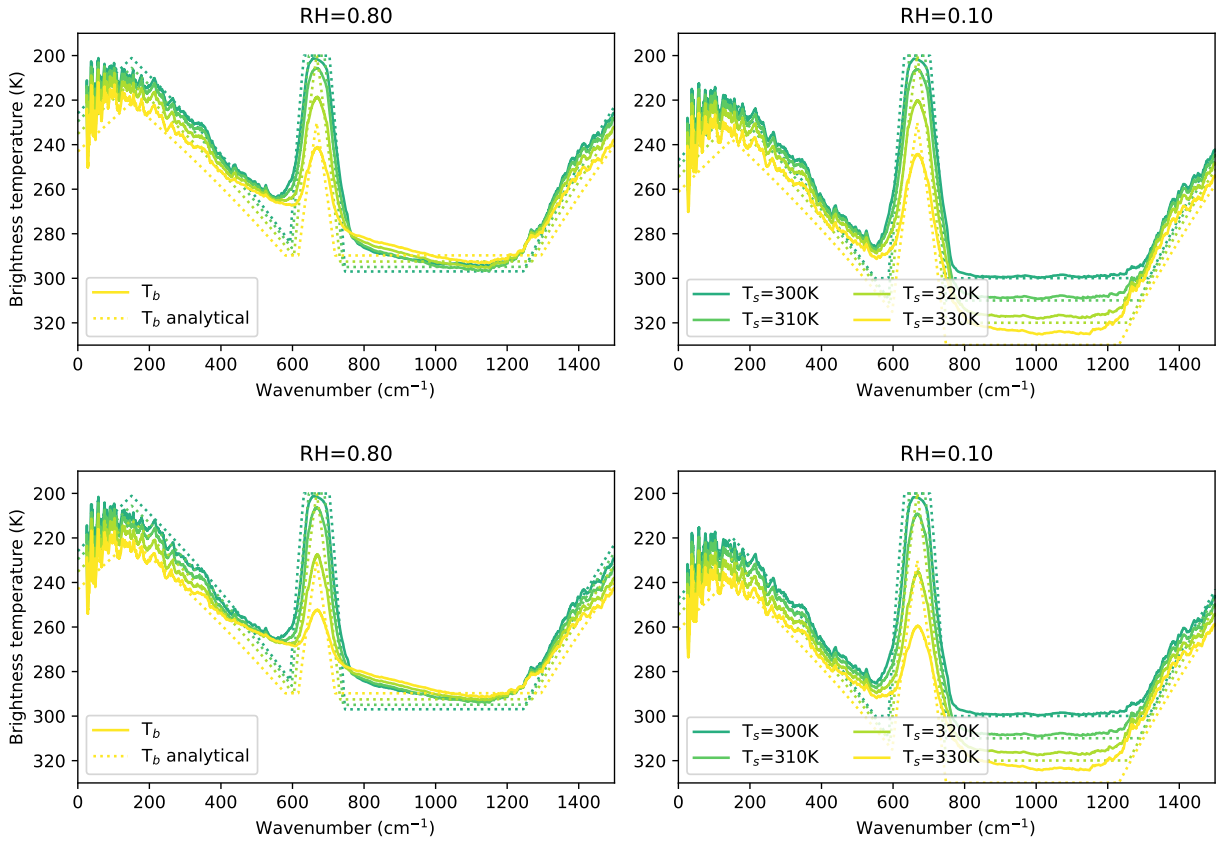

FIG. B1. Brightness temperatures computed from line-by-line calculations and smoothed with a 50 cm^{-1} median filter (solid), versus analytical emission temperatures (dashed). Top row: calculations use a bulk lapse-rate profile, $T(p) = T_s(p/p_s)^{\gamma_{\rm lr}}$. Bottom row: calculations use a moist adiabat.

At high surface temperatures the CO_2 band center transitions from mainly radiating from the stratosphere to mainly radiating from the troposphere. Figure B1 shows smoothed brightness temperatures T_b computed from the 1D line-by-line calculations described in Section 5, with a CO_2 volume-mixing ratio of 400 ppm. In the middle of the CO_2 band, at about 667 cm^{-1}, CO_2 radiates from the troposphere at surface temperatures above $\sim$ 310 K. In rough agreement with

the line-by-line results, our analytical CO_2 brightness temperatures predict this transition happens at a surface temperature of $\sim$ 320 K (dashed lines in Fig. B1). In practice we therefore use a transition temperature of $T_{s,0} = 310$ K for 400 ppm of CO_2 to determine when CO_2 changes from a stratospheric to a tropospheric radiator.

APPENDIX C

Impact of realistic lapse rates on λ_{LW}

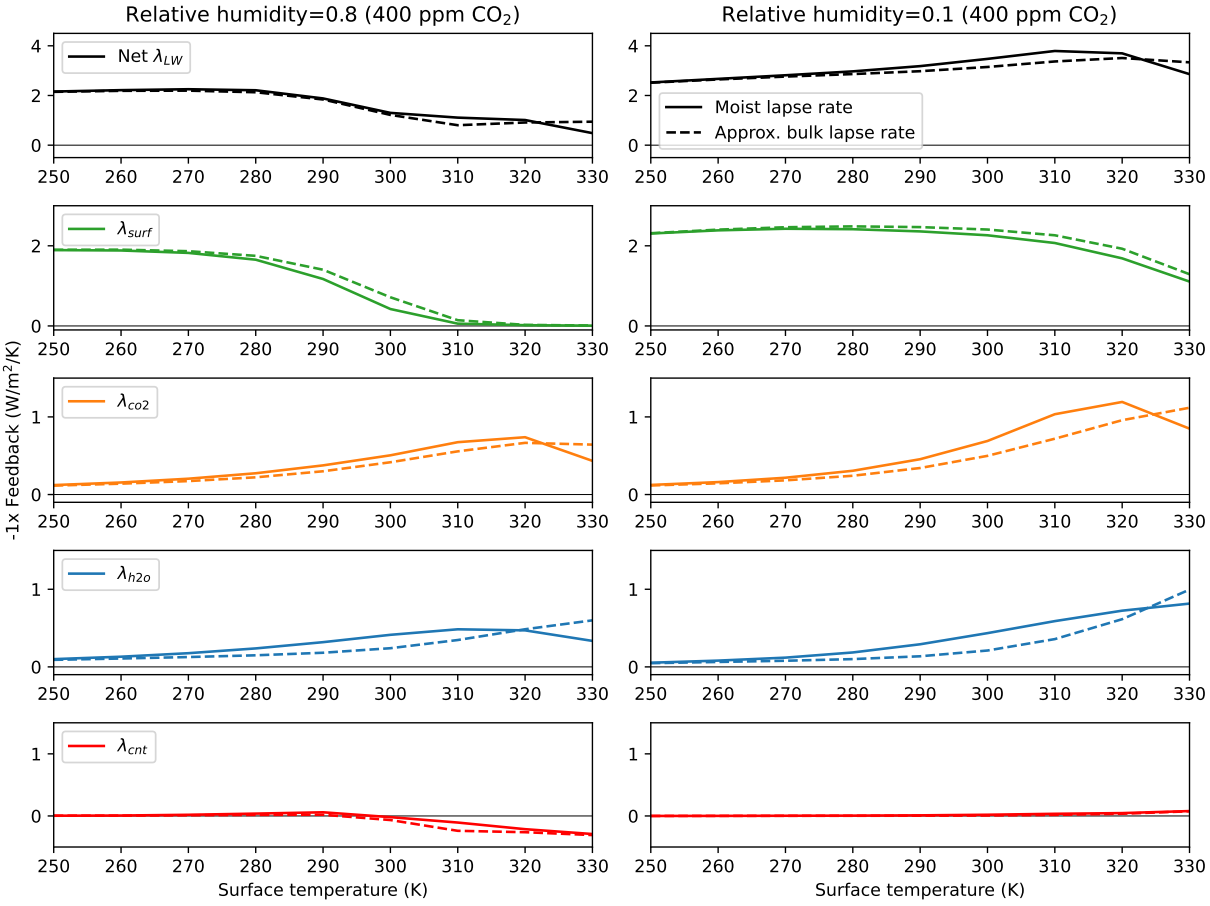

FIG. C1. The impact of the bulk lapse rate approximation on longwave feedbacks is modest below ~320 K, but becomes significant at high temperatures. Solid lines are numerical feedbacks calculated assuming the atmosphere follows a moist adiabatic profile, dashed lines are numerical feedbacks calculated assuming the atmosphere follows our bulk lapse rate approximation. Note the change in y-axes between different rows.

Figure C1 compares a set of 1D calculations with a moist adiabat to a set of numerical calculations that fixes the atmospheric temperature-pressure profile according to our bulk lapse rate approximation. The lapse rate approximation only has a small impact on λ_{LW} at surface temperatures below 300 K. The error in individual feedbacks is more significant below 300 K, which means errors in surface and atmospheric feedbacks due to differences in the lapse rate γ_{lr} largely cancel. The cancellation of errors can be partly explained by the effect of γ_{lr} on the atmospheric water vapor path. For example, an erroneously large value for γ_{lr} means the upper atmosphere is too cold, and thus contains less water vapor, than a realistic moist adiabat. This shrinks the width of the window region while increasing the width of the H_2O bands, which renders λ_{surf} too large and λ_{H_2O} too small, in line with the results shown in Figure C1.

The impact of the bulk lapse rate approximation becomes more significant above 300 K, with clear errors in the temperature-dependence of individual feedbacks above 320 K. Overall, we therefore consider the bulk lapse rate approximation suitable for approximating λ_{LW} below $\sim$ 320 K.

References

Andrews, T., J. M. Gregory, and M. J. Webb, 2015: The Dependence of Radiative Forcing and Feedback on Evolving Patterns of Surface Temperature Change in Climate Models. *Journal of Climate*, **28 (4)**, 1630–1648, https://doi.org/10.1175/JCLI-D-14-00545.1.

Andrews, T., J. M. Gregory, M. J. Webb, and K. E. Taylor, 2012: Forcing, feedbacks and climate sensitivity in CMIP5 coupled atmosphere-ocean climate models. *Geophysical Research Letters*, **39 (9)**, https://doi.org/10.1029/2012GL051607.

Andrews, T., and Coauthors, 2018: Accounting for Changing Temperature Patterns Increases Historical Estimates of Climate Sensitivity. *Geophysical Research Letters*, **45 (16)**, 8490–8499, https://doi.org/10.1029/2018GL078887.

Armour, K. C., C. M. Bitz, and G. H. Roe, 2013: Time-Varying Climate Sensitivity from Regional Feedbacks. *Journal of Climate*, **26 (13)**, 4518–4534, https://doi.org/10.1175/JCLI-D-12-00544.1.

Bloch-Johnson, J., M. Rugenstein, and D. S. Abbot, 2020: Spatial radiative feedbacks from internal variability using multiple regression. *Journal of Climate*, https://doi.org/10.1175/JCLI-D-19-0396.1.

Boeke, R. C., P. C. Taylor, and S. A. Sejas, 2021: On the Nature of the Arctic's Positive Lapse-Rate Feedback. *Geophysical Research Letters*, **48 (1)**, e2020GL091 109, https://doi.org/10.1029/2020GL091109.

Bretherton, C. S., P. N. Blossey, and M. Khairoutdinov, 2005: An Energy-Balance Analysis of Deep Convective Self-Aggregation above Uniform SST. *Journal of the Atmospheric Sciences*, **62 (12)**, 4273–4292, https://doi.org/10.1175/JAS3614.1.

Budyko, M. I., 1969: The effect of solar radiation variations on the climate of the Earth. *Tellus*, **21 (5)**, 611–619, https://doi.org/10.1111/j.2153-3490.1969.tb00466.x.

Cai, M., and J. Lu, 2009: A new framework for isolating individual feedback processes in coupled general circulation climate models. Part II: Method demonstrations and comparisons. *Climate Dynamics*, **32 (6)**, 887–900, https://doi.org/10.1007/s00382-008-0424-4.

Chung, E.-S., B. J. Soden, and B.-J. Sohn, 2010: Revisiting the determination of climate sensitivity from relationships between surface temperature and radiative fluxes. *Geophysical Research Letters*, **37 (10)**, https://doi.org/10.1029/2010GL043051.

Collins, W. J., and Coauthors, 2011: Development and evaluation of an Earth-System model – HadGEM2. *Geoscientific Model Development*, **4 (4)**, 1051–1075, https://doi.org/10.5194/gmd-4-1051-2011.

Crisp, D., S. B. Fels, and M. D. Schwarzkopf, 1986: Approximate methods for finding CO2 15-Mm band transmission in planetary atmospheres. *Journal of Geophysical Research: Atmospheres*, **91 (D11)**, 11 851–11 866, https://doi.org/10.1029/JD091iD11p11851.

Cronin, T. W., and M. F. Jansen, 2016: Analytic radiative-advective equilibrium as a model for high-latitude climate. *Geophysical Research Letters*, **43 (1)**, 2015GL067 172, https://doi.org/10.1002/2015GL067172.

Ding, F., and R. T. Pierrehumbert, 2016: Convection in Condensible-rich Atmospheres. *The Astrophysical Journal*, **822 (1)**, 24, https://doi.org/10.3847/0004-637X/822/1/24.

Feldl, N., and G. H. Roe, 2013: Four perspectives on climate feedbacks. *Geophysical Research Letters*, **40 (15)**, 4007–4011, https://doi.org/10.1002/grl.50711.

Goldblatt, C., T. D. Robinson, K. J. Zahnle, and D. Crisp, 2013: Low simulated radiation limit for runaway greenhouse climates. *Nature Geoscience*, **6 (8)**, 661–667, https://doi.org/10.1038/ngeo1892.

Gordon, I. E., and Coauthors, 2017: The HITRAN2016 molecular spectroscopic database. *Journal of Quantitative Spectroscopy and Radiative Transfer*, **203**, 3–69, https://doi.org/10.1016/j.jqsrt.2017.06.038.

Hartmann, D. L., and K. Larson, 2002: An important constraint on tropical cloud - climate feedback. *Geophysical Research Letters*, **29 (20)**, 12–1–12–4, https://doi.org/10.1029/2002GL015835.

Held, I. M., and K. M. Shell, 2012: Using Relative Humidity as a State Variable in Climate Feedback Analysis. *Journal of Climate*, **25 (8)**, 2578–2582, https://doi.org/10.1175/JCLI-D-11-00721.1.

Henry, M., and T. M. Merlis, 2019: The Role of the Nonlinearity of the Stefan–Boltzmann Law on the Structure of Radiatively Forced Temperature Change. *Journal of Climate*, **32 (2)**, 335–348, https://doi.org/10.1175/JCLI-D-17-0603.1.

Hersbach, H., and Coauthors, 2020: The ERA5 global reanalysis. *Quarterly Journal of the Royal Meteorological Society*, **146 (730)**, 1999–2049, https://doi.org/10.1002/qj.3803.

Huang, J., 2018: A Simple Accurate Formula for Calculating Saturation Vapor Pressure of Water and Ice. *Journal of Applied Meteorology and Climatology*, **57 (6)**, 1265–1272, https://doi.org/10.1175/JAMC-D-17-0334.1.

Huang, X., X. Chen, B. J. Soden, and X. Liu, 2014: The spectral dimension of longwave feedback in the CMIP3 and CMIP5 experiments. *Geophysical Research Letters*, **41 (22)**, 7830–7837, https://doi.org/10.1002/2014GL061938.

Huang, Y., S. Leroy, P. J. Gero, J. Dykema, and J. Anderson, 2010: Separation of longwave climate feedbacks from spectral observations. *Journal of Geophysical Research: Atmospheres*, **115 (D7)**, https://doi.org/10.1029/2009JD012766.

Ingram, W., 2010: A very simple model for the water vapour feedback on climate change. *Quarterly Journal of the Royal Meteorological Society*, **136 (646)**, 30–40, https://doi.org/10.1002/qj.546.

Jeevanjee, N., and S. Fueglistaler, 2020: Simple Spectral Models for Atmospheric Radiative Cooling. *Journal of the Atmospheric Sciences*, **77 (2)**, 479–497, https://doi.org/10.1175/JAS-D-18-0347.1.

Jeevanjee, N., D. D. B. Koll, and N. Lutsko, 2021a: "Simpson's Law" and the Spectral Cancellation of Climate Feedbacks. *Geophysical Research Letters*, **48 (14)**, e2021GL093 699, https://doi.org/10.1029/2021GL093699.

Jeevanjee, N., J. T. Seeley, D. Paynter, and S. Fueglistaler, 2021b: An Analytical Model for Spatially Varying Clear-Sky CO2 Forcing. *Journal of Climate*, **34 (23)**, 9463–9480, https://doi.org/10.1175/JCLI-D-19-0756.1.

Kluft, L., S. Dacie, M. Brath, S. A. Buehler, and B. Stevens, 2021: Temperature-Dependence of the Clear-Sky Feedback in Radiative-Convective Equilibrium. *Geophysical Research Letters*, **48 (22)**, e2021GL094 649, https://doi.org/10.1029/2021GL094649.

Kluft, L., S. Dacie, S. A. Buehler, H. Schmidt, and B. Stevens, 2019: Re-Examining the First Climate Models: Climate Sensitivity of a Modern Radiative–Convective Equilibrium Model. *Journal of Climate*, **32 (23)**, 8111–8125, https://doi.org/10.1175/JCLI-D-18-0774.1.

Koll, D. D. B., and T. W. Cronin, 2018: Earth's outgoing longwave radiation linear due to H2O greenhouse effect. *Proceedings of the National Academy of Sciences*, **115 (41)**, 10 293–10 298, https://doi.org/10.1073/pnas.1809868115, https://www.pnas.org/content/115/41/10293.full.pdf.

Koll, D. D. B., and T. W. Cronin, 2019: Hot Hydrogen Climates Near the Inner Edge of the Habitable Zone. *The Astrophysical Journal*, **881 (2)**, 120, https://doi.org/10.3847/1538-4357/ab30c4, 1907.13169.

Manabe, S., and R. T. Wetherald, 1967: Thermal Equilibrium of the Atmosphere with a Given Distribution of Relative Humidity. *Journal of the Atmospheric Sciences*, **24**, 241–259, https://doi.org/10.1175/1520-0469(1967)024<0241:TEOTAW>2.0.CO;2.

McKim, B. A., N. Jeevanjee, and G. K. Vallis, 2021: Joint Dependence of Longwave Feedback on Surface Temperature and Relative Humidity. *Geophysical Research Letters*, **48 (18)**, e2021GL094 074, https://doi.org/10.1029/2021GL094074.

Meraner, K., T. Mauritsen, and A. Voigt, 2013: Robust increase in equilibrium climate sensitivity under global warming. *Geophysical Research Letters*, **40 (22)**, 5944–5948, https://doi.org/10.1002/2013GL058118.

Mlawer, E. J., V. H. Payne, J.-L. Moncet, J. S. Delamere, M. J. Alvarado, and D. C. Tobin, 2012: Development and recent evaluation of the MT_CKD model of continuum absorption. *Phil. Trans. R. Soc. A*, **370 (1968)**, 2520–2556, https://doi.org/10.1098/rsta.2011.0295.

Pan, F., and X. Huang, 2018: The Spectral Dimension of Modeled Relative Humidity Feedbacks in the CMIP5 Experiments. *Journal of Climate*, **31 (24)**, 10 021–10 038, https://doi.org/10.1175/JCLI-D-17-0491.1.

Payne, A. E., M. F. Jansen, and T. W. Cronin, 2015: Conceptual model analysis of the influence of temperature feedbacks on polar amplification. *Geophysical Research Letters*, **42 (21)**, 2015GL065 889, https://doi.org/10.1002/2015GL065889.

Pierrehumbert, R., 1995: Thermostats, radiator fins and the local runaway greenhouse. *Journal of the Atmospheric Sciences*, **52**, 1784–1806.

Pierrehumbert, R. T., 2010: *Principles of Planetary Climate*. Cambridge University Press, Cambridge, UK.

Raghuraman, S. P., D. Paynter, and V. Ramaswamy, 2019: Quantifying the Drivers of the Clear Sky Greenhouse Effect, 2000–2016. *Journal of Geophysical Research: Atmospheres*, **n/a (n/a)**, https://doi.org/10.1029/2019JD031017.

Ramirez, R. M., R. K. Kopparapu, V. Lindner, and J. F. Kasting, 2014: Can Increased Atmospheric CO2 Levels Trigger a Runaway Greenhouse? *Astrobiology*, **14 (8)**, 714–731, https://doi.org/10.1089/ast.2014.1153.

Romps, D. M., 2016: Clausius–Clapeyron Scaling of CAPE from Analytical Solutions to RCE. *Journal of the Atmospheric Sciences*, **73 (9)**, 3719–3737, https://doi.org/10.1175/JAS-D-15-0327.1.

Romps, D. M., J. T. Seeley, and J. P. Edman, 2022: Why the forcing from carbon dioxide scales as the logarithm of its concentration. *Journal of Climate*, **-1 (aop)**, 1–60, https://doi.org/10.1175/JCLI-D-21-0275.1.

Seeley, J. T., and N. Jeevanjee, 2021: H2O Windows and CO2 Radiator Fins: A Clear-Sky Explanation for the Peak in Equilibrium Climate Sensitivity. *Geophysical Research Letters*, **48 (4)**, e2020GL089 609, https://doi.org/10.1029/2020GL089609.

Seeley, J. T., N. Jeevanjee, W. Langhans, and D. M. Romps, 2019: Formation of Tropical Anvil Clouds by Slow Evaporation. *Geophysical Research Letters*, **46 (1)**, 492–501, https://doi.org/10.1029/2018GL080747.

Sherwood, S., and Coauthors, 2020: An assessment of Earth's climate sensitivity using multiple lines of evidence. *Reviews of Geophysics*, **n/a (n/a)**, e2019RG000 678, https://doi.org/10.1029/2019RG000678.

Simpson, G. C., 1928: Further studies in terrestrial radiation. *Memoirs of the Royal Meteorological Society*, **3 (21)**.

Soden, B. J., I. M. Held, R. Colman, K. M. Shell, J. T. Kiehl, and C. A. Shields, 2008: Quantifying Climate Feedbacks Using Radiative Kernels. *Journal of Climate*, **21 (14)**, 3504–3520, https://doi.org/10.1175/2007JCLI2110.1.

Stuecker, M. F., and Coauthors, 2018: Polar amplification dominated by local forcing and feedbacks. *Nature Climate Change*, **8 (12)**, 1076, https://doi.org/10.1038/s41558-018-0339-y.

Tierney, J. E., J. Zhu, J. King, S. B. Malevich, G. J. Hakim, and C. J. Poulsen, 2020: Glacial cooling and climate sensitivity revisited. *Nature*, **584 (7822)**, 569–573, https://doi.org/10.1038/s41586-020-2617-x.

Vallis, G. K., P. Zurita-Gotor, C. Cairns, and J. Kidston, 2014: Response of the large-scale structure of the atmosphere to global warming. *Quarterly Journal of the Royal Meteorological Society*, n/a–n/a, https://doi.org/10.1002/qj.2456.

Wilson, D. J., and J. Gea-Banacloche, 2012: Simple model to estimate the contribution of atmospheric CO2 to the Earth's greenhouse effect. *American Journal of Physics*, **80 (4)**, 306–315, https://doi.org/10.1119/1.3681188.

Zelinka, M. D., T. A. Myers, D. T. McCoy, S. Po-Chedley, P. M. Caldwell, P. Ceppi, S. A. Klein, and K. E. Taylor, 2020: Causes of Higher Climate Sensitivity in CMIP6 Models. *Geophysical Research Letters*, **47 (1)**, e2019GL085 782, https://doi.org/10.1029/2019GL085782.

Zhang, R., H. Wang, Q. Fu, and P. J. Rasch, 2020a: Assessing Global and Local Radiative Feedbacks Based on AGCM Simulations for 1980–2014/2017. *Geophysical Research Letters*, **47 (12)**, e2020GL088 063, https://doi.org/10.1029/2020GL088063.

Zhang, Y., N. Jeevanjee, and S. Fueglistaler, 2020b: Linearity of Outgoing Longwave Radiation: From an Atmospheric Column to Global Climate Models. *Geophysical Research Letters*, **47 (17)**, e2020GL089 235, https://doi.org/10.1029/2020GL089235.